








Radiative Driving of the AGN Outflows in the Narrow-Line Seyfert 1 Galaxy NGC 4051^{*†}BEENA MEENA ¹, D. MICHAEL CRENSHAW ¹, HENRIQUE R. SCHMITT ², MITCHELL REVALSKI ³,
TRAVIS C. FISCHER ⁴, GARRETT E. POLACK ¹, STEVEN B. KRAEMER ⁵, AND DZHULIYA DASHTAMIROVA ³¹*Department of Physics and Astronomy, Georgia State University, 25 Park Place, Suite 605, Atlanta, GA 30303, USA*²*Naval Research Laboratory, Washington, DC 20375, USA*³*Space Telescope Science Institute, 3700 San Martin Drive, Baltimore, MD 21218, USA*⁴*AURA for ESA, Space Telescope Science Institute, 3700 San Martin Drive, Baltimore, MD 21218, USA*⁵*Institute for Astrophysics and Computational Sciences, Department of Physics, The Catholic University of America, Washington, DC 20064, USA*

(Accepted May 13, 2021)

ABSTRACT

We explore the properties of ionized gas in the nuclear and circumnuclear environment of the narrow-line Seyfert 1 galaxy NGC 4051 using spectroscopic and imaging observations from the *Hubble Space Telescope* (*HST*) and Apache Point Observatory (APO)’s ARC 3.5m Telescope. We identify an unresolved moderate-density intermediate width component and a high-density broad component in the optical emission lines from the active nucleus, as well as spatially-resolved emission extending up to ~ 1 kpc in the AGN ionized narrow-line region (NLR) and ~ 8 kpc in the stellar ionized host galaxy. The *HST* narrow-band image reveals a distinct conical structure in [O III] emission towards the NE, and the ionized gas kinematics shows up to two blueshifted velocity components, indicating outflows along the edges of a cone. We introduce an improved model of biconical outflow, with our line of sight passing through the wall of the cone, which suggests that the large number of outflowing UV absorbers seen in NGC 4051 are NLR clouds in absorption. Using the de-projection factors from the biconical geometry, we measure true outflow velocities up to 680 km s^{-1} at a distance of ~ 350 pc, however, we do not find any rotational signature inside a projected distance $\leq 10''$ (~ 800 pc) from the nucleus. We compare the gas kinematics with analytical models based on a radiation-gravity formalism, which show that most of the observed NLR outflows are launched within ~ 0.5 pc of the nucleus and can travel up to ~ 1 kpc from this low-luminosity AGN.

Keywords: galaxies: active — galaxies: individual (NGC 4051) — galaxies: kinematics and dynamics — galaxies: Seyfert – ISM: jets and outflows

1. INTRODUCTION

1.1. AGN Driven Feedback

Active Galactic Nuclei (AGN) are powered by supermassive black holes (SMBHs) with masses $\geq 10^6 M_\odot$ that are feeding on the surrounding gas at the centers of their host galaxies. This feeding process creates massive amounts of electromagnetic radiation from the accretion disk of the SMBH that can lead to AGN feedback. This feedback is usually detected in the form of jets and/or winds (Crenshaw et al. 2003; Fabian 2012; King & Pounds 2015; Blandford et al. 2019). Jets are collimated beams

Corresponding author: Beena Meena
bmeena@astro.gsu.edu

^{*} Based on observations made with the NASA/ESA Hubble Space Telescope, obtained from the Data Archive at the Space Telescope Science Institute, which is operated by the Association of Universities for Research in Astronomy, Inc., under NASA contract NAS 5-26555. These observations are associated with program No. 8253, 12212.

[†] Based in part on observations obtained with the Apache Point Observatory 3.5-meter telescope, which is owned and operated by the Astrophysical Research Consortium.

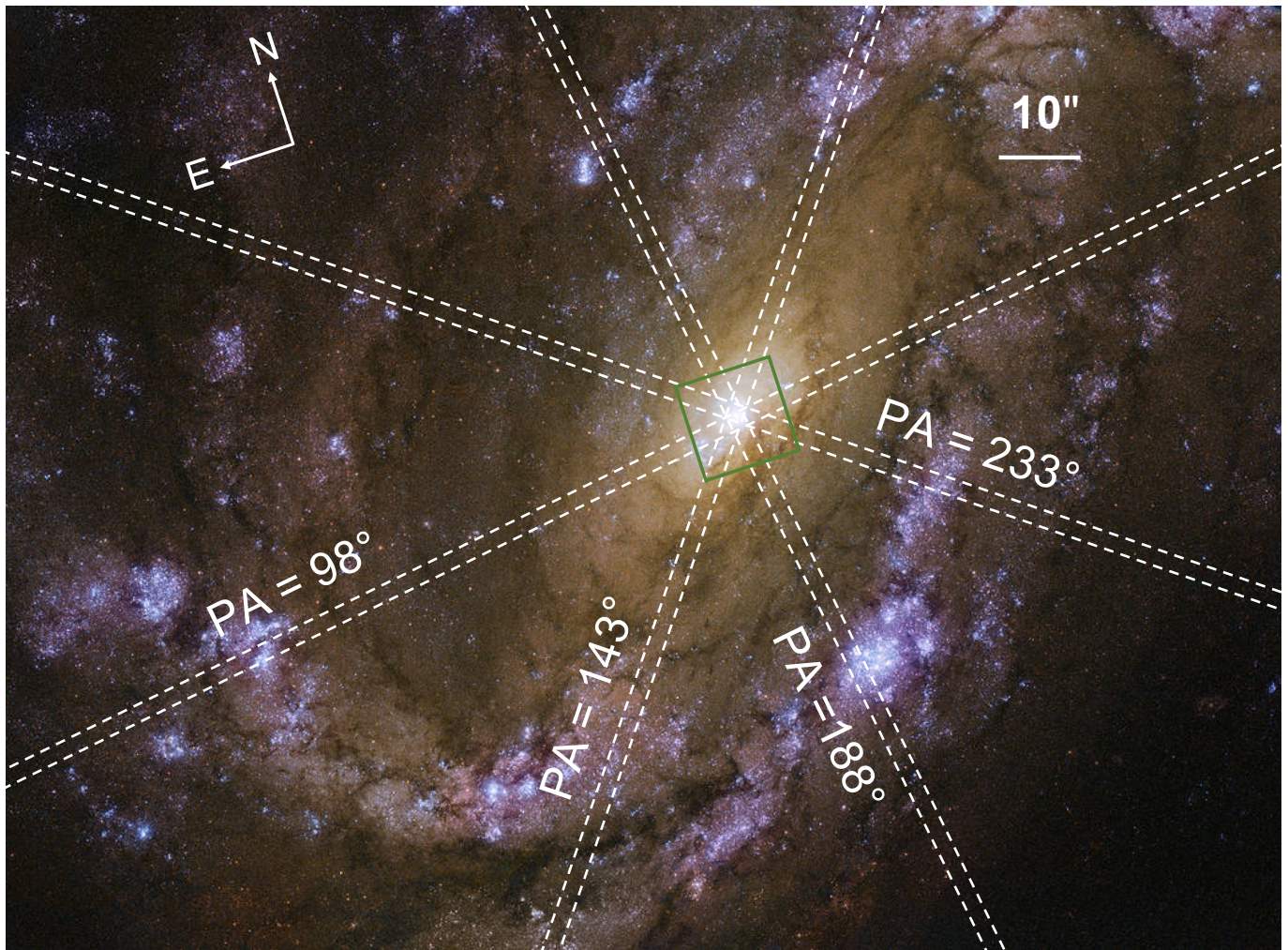


Figure 1. A $2.60' \times 1.93'$ color-composite image of NGC 4051 using multiple *HST* WFC3 filters. The image shows the orientation of the host galaxy, spiral arms, and the star forming regions. The [O III] ionized gas inside the $12'' \times 12''$ green box at the center is shown in Figure 2. North is 18° counter-clockwise, and the $2''$ -wide APO slits are overlaid and labeled with their position angles. Image credit: NASA/ESA/Hubble, D. M. Crenshaw and O. Fox.

of extremely high energy particles that travel at relativistic speeds and can impact large-scale extragalactic environments. AGN driven winds are outflows of ionized (Storchi-Bergmann et al. 2010; Laha et al. 2021), neutral (Rupke et al. 2005, 2017), and/or molecular (Veilleux et al. 2017; Herrera-Camus et al. 2019) gas that can be produced by the interaction of radiation from the accretion disk around the SMBH with the surrounding matter. They predominantly influence the nuclear and circum-nuclear regions of their host galaxies. These outflows can push the fueling gas away from the nucleus, and propagate kinetic energy into the interstellar medium, thereby disrupting potentially star-forming gas. Consequently, this feeding-feedback mechanism may regulate the growth of SMBHs and the properties of the galactic bulge, possibly explaining empirical relationships such as the BH mass - bulge luminosity ($M_\bullet - L_{bulge}$: Kormendy

& Richstone 1995; Magorrian et al. 1998; Marconi & Hunt 2003) and BH mass - bulge stellar velocity dispersion ($M_\bullet - \sigma_*$: Ferrarese & Merritt 2000; Gebhardt et al. 2000; Kormendy & Ho 2013) of the present day universe.

The ionized gas outflows are often observed in X-ray & UV absorption (Crenshaw & Kraemer 2005; Costantini 2010; Crenshaw & Kraemer 2012) and optical emission lines in the narrow-line regions (NLRs) of nearby Seyfert galaxies (Veilleux & Osterbrock 1987; Veilleux 1991; Colbert et al. 1996; Nelson et al. 2000; Fischer et al. 2013). These outflows have been seen in a roughly biconical or hourglass structure (Antonucci & Miller 1985; Pogge 1988; Schmitt & Kinney 1996; Arribas et al. 1996; Hutchings et al. 1998; Storchi-Bergmann et al. 2018; May et al. 2020), shaped by the thick torus of gas and dust around the central engine. Spectroscopic observations have shown that the central AGN can radiatively excite

and drive the outflowing clouds to hundreds of parsecs or more with velocities up to $\sim 2000 \text{ km s}^{-1}$ (Crenshaw & Kraemer 2000; Crenshaw et al. 2000; Das et al. 2005; Müller-Sánchez et al. 2011). At larger distances, the AGN may ionize gas that is part of the galaxy without pushing it outwards or creating outflows, in a region that has been conventionally defined as the extended narrow-line region (ENLR, Unger et al. 1987).

It is important to quantify the outflow properties in order to investigate the feedback efficiency of the AGN. The physical conditions of the gas in the NLR and ENLR, such as density and temperature, can be estimated using photoionization models (Ferland et al. 1998; Kraemer et al. 2008), while calculations of mass outflow rates (Crenshaw et al. 2015; Revalski et al. 2018a,b; Trindade Falcão et al. 2020; Revalski et al. 2021) give us direct measurements of gas removal and kinetic energy deposition into the ambient medium of the host galaxy bulges. These studies require accurate measurements of travel distances and space velocities to calculate the gas evacuation time scales.

The anatomy of AGN driven outflows has been widely studied using optical imaging and spatially resolved kinematics of emission lines such as [O III] $\lambda 5007$ and $H\alpha$ $\lambda 6563$. Using these emission lines, Fischer et al. (2013) identified non-circular velocities in the NLR and derived geometric models (Crenshaw & Kraemer 2000; Crenshaw et al. 2000; Das et al. 2005) of ionized gas outflows for a sample of nearby Seyfert galaxies. Recent studies have found that the radial extent of the photoionized gas (NLR + ENLR) roughly scales with the NLR luminosity (Bennert et al. 2002; Schmitt et al. 2003; Ganguly & Brotherton 2008; Mullaney et al. 2013; Karouzos et al. 2016; Storchi-Bergmann et al. 2018); however the sizes of AGN ionized outflows are shown to be smaller than the entire emission line regions and bulge radii (Karouzos et al. 2016; Kang & Woo 2018; Fischer et al. 2018). By measuring the velocity dispersion of [O III] ionized gas, Fischer et al. (2018) suggested that even though nearby AGN driven outflows may not be powerful enough to clear the full extents of the bulges (Revalski et al. 2018a,b; Trindade Falcão et al. 2020), they could still disrupt and redistribute a significant fraction of potential star forming gas in the system.

Previously, we have explored the origins of AGN outflows by developing dynamical models (Das et al. 2007) based on radiation pressure mechanisms and the gravitational drag of the host galaxy. Using these models, Fischer et al. (2017), showed that outflows in the high luminosity Seyfert 2 galaxy Mrk 573 ($\log(L_{bol}) = 45.5 \pm 0.6 \text{ erg s}^{-1}$; Meléndez et al. 2008b,a; Kraemer et al. 2009) can be launched from as far out as 500 pc due to in-

situ ionization and acceleration of gas in the plane of the host galaxy. They later found that these launch distances are even larger (Fischer et al. 2019) for the lower mass Seyfert 2 galaxy 2MASX J04234080+0408017, abbreviated as 2MASX J0423 ($\log(L_{bol}) = 45.55 \pm 0.3 \text{ erg s}^{-1}$), where the outflows can be driven from tens of thousands of parsecs encompassing the entire emitting field. Similar methods have been recently followed by (García-Bernete et al. 2021) for the intermediate luminosity AGN of NGC 5643 ($\log(L_{bol}) = 43.9 \text{ erg s}^{-1}$), showing that almost all of the observed gas originated from the inner 16 pc.

To expand our understating of outflow properties and determine whether an AGN mass/luminosity scaling factor is involved, we systematically study the morphology of ionized gas outflows and radiative efficiency of a low mass, low luminosity ($L_{bol} \approx 10^{43} \text{ erg s}^{-1}$) AGN in the nearby narrow-line Seyfert 1 (NLS1) galaxy NGC 4051. In the future, we will include more targets in our sample and carry out a similar analysis to further explore the relationships between AGN, host galaxy, and outflow parameters.

1.2. NGC 4051

NGC 4051 is an SAB(rs)bc galaxy at a redshift of $z = 0.00234$ (de Vaucouleurs et al. 1991; Verheijen & Sancisi 2001). A color image of the galaxy is shown in Figure 1. The distance measurements for this galaxy range from 8.8 Mpc to 17.0 Mpc (NASA/IPAC Extragalactic Database). For our work, we adopted a distance of $16.6 \pm 0.3 \text{ Mpc}$ from Cepheid-based measurements (Yuan et al. 2020) so that its transverse scale corresponds to $\sim 80 \text{ pc}''$ on the plane of the sky. It is classified as a NLS1 based on the low [O III]/ $H\beta$ (broad plus narrow) ratio in the nuclear regions (Osterbrock & Pogge 1985; Leighly 1999) and the observed width of broad line region (BLR) $H\beta$ emission line with full-width at half-maximum (FWHM) $< 3000 \text{ km s}^{-1}$, which is smaller than typical type 1 Seyfert galaxies. The AGN of this galaxy hosts a SMBH with a mass of $\log(M_{BH}) = 6.13^{+0.12}_{-0.15} M_{\odot}$ (Bentz & Manne-Nicholas 2018) and is highly variable in optical and X-ray observations (Peterson et al. 2000; Breedt et al. 2010). An estimated bolometric luminosity of $\log(L_{bol}) = 42.95 \text{ erg s}^{-1}$ (Denney et al. 2009; Bentz et al. 2009, 2013) has been reported based on $\lambda L_{\lambda}(5100\text{Å})$ measurements. With this mass and luminosity, the AGN is radiating at approximately 5% of the Eddington luminosity ($L/L_{edd} \approx 0.053$) as noted by Peterson et al. (2004).

The AGN driven outflows in NGC 4051 has been extensively studied in X-ray and UV absorption lines (Collinge et al. 2001; Kraemer et al. 2012; Crenshaw & Kraemer 2012; Laha et al. 2014). In addition to the warm ab-

sorbers, X-ray ultra fast outflows (UFOs) and shocked outflows have been reported (Pounds & Vaughan 2011; Pounds & King 2013; Laha et al. 2016; King & Pounds 2015) in momentum-driven winds. In the optical, the ionized gas outflows have been detected in both narrow Balmer and forbidden emission lines. Ground-based [O III] images show an unresolved nucleus with faint emission (Haniff et al. 1988; Pogge 1989) that co-aligns with the strong nuclear radio structure at 100° in the SE. Schmitt & Kinney (1996) verify similar emission in an *HST* Wide Field Planetary Camera (WFPC) - F502N image. Using a Manchester Echelle Spectrograph (MES) image, Christophoulou et al. (1997) discovered a $9''$ long wedge shaped ionized emission in [O III] that bisects at 33° . Spectroscopic observations using the same instrument provided a model for conical outflow that is inclined at 50° from line of sight with a half opening angle of 25° . GEMINI GMOS-IFU observations show outflows with strong flux in the west to east direction close to the nucleus, but more extended towards the north with velocities reaching up to 500 km s^{-1} (Barbosa et al. 2009). Fischer et al. (2013) developed a kinematic model for a biconical outflow in NGC 4051 using *HST* STIS spectra that is directed towards position angle (PA) 80° NE with a maximum half opening angle of 25° .

In this work we present our improved understanding of the NLR in NGC 4051, including the extent and morphology of the outflows, and investigate the significance of AGN radiation pressure driving. We describe the imaging and spectroscopic observations from *HST* and APO (§2), spectroscopic analysis (§3), results including the ionized gas kinematics (§4.1 and 4.2), emission line diagnosis (§4.3), and the revised outflow model (§4.4). Finally we compare the kinematics with analytical models of radiative acceleration-gravitation deceleration (§4.5), discuss (§5) and conclude (§6) the observed results.

2. OBSERVATIONS

2.1. Hubble Space Telescope (*HST*)

We used archival observations of NGC 4051 from the *Hubble Space Telescope* (*HST*)’s Space Telescope Imaging Spectrograph (STIS) and Wide Field Camera 3 (WFC3). We retrieved the calibrated data from the Mikulski Archive at the Space Telescope Science Institute (MAST) and processed and combined them into the final data files using the Interactive Data Language (IDL). Additional details of post-data reduction and calibration are given in Fischer et al. (2013). The WFC3 combined and drizzled images from the Hubble legacy Archive (HLA) were analysed using SAOImage DS9 and the Astropy library in Python (Smithsonian Astrophysical Observatory 2000; Astropy Collaboration et al. 2013). The STIS

observations were retrieved under Hubble program ID 8253 (PI: M. Whittle) and the WFC3 images from program ID 12212 (PI: D. M. Crenshaw). A summary of the *HST* observations is provided in Table 1.

To investigate the kinematics of emission line clouds in the NLR of NGC 4051, we used the long-slit spectra from the medium dispersion G430M grating (resolving power $R \approx 9000$), which provides a spectral resolution of 0.56 \AA in the dispersion direction and a spatial resolution of $0''.10$ in the cross-dispersion direction. Two parallel $52'' \times 0''.2$ long slits observations were available along a PA of 89.8° . For an extended source filling the slit in the dispersion direction, the effective spectral resolving power is reduced to $R \approx 4500$ (FWHM $\approx 67 \text{ km s}^{-1}$). The two slits are at offsets of $0''.05$ south (labeled “A”) and $0''.20$ north (labeled “B”) from the nucleus. The spectra extracted along each slit contain the strong [O III] $\lambda\lambda 4959, 5007$ lines, which trace the AGN ionized gas in a part of the NLR with high angular contrast. The STIS slit positions and offsets are shown in Figure 2.

We supplemented our long-slit spectroscopic observations with a narrow-band image available for the F502N filter on WFC3, displayed in Figure 2, to study the morphology of the emission line regions. The high resolution (pixel scale of $0''.039 \text{ pixel}^{-1}$) image was taken using the Ultraviolet-Visible (UVIS) detector with a field of view (FOV) of $162'' \times 162''$. The F502N image contains sufficiently strong [O III] emission, to compare with our spectroscopic analysis and to map the circumnuclear ionized gas in NGC 4051. We used a F547M image (from the same program ID) to subtract the continuum from the line emission. The final image was cropped to $12'' \times 12''$ as shown in Figure 2 to highlight the structure of the [O III] emission in the NLR.

2.2. Apache Point Observatory (*APO*)

We have previously observed extended ionized emission using relatively wide long slits in ground-based observations of Mrk 573 (Fischer et al. 2017; Revalski et al. 2018a), Mrk 34 (Revalski et al. 2018b), Mrk 3 (Gnilka et al. 2020), and Mrk 78 (Revalski et al. 2021). These observations allow us to detect fainter emission in the ENLR and host galaxy from ionized gas at larger distances that were undetectable with narrow *HST* STIS slits.

To accurately measure the extent of the ionized gas and AGN driven outflows, we use $6' \times 2''$ wide slits on the Apache Point Observatory (*APO*)’s 3.5 meter telescope with its Dual Imaging Spectrograph (DIS). The long slit covers the ionized gas from the host galaxy on large scales, allowing us to identify the rotation curve of NGC 4051.

Table 1. *HST* Observations of NGC 4051

Instrument Name	Proposal ID	Observation ID	Date (UT)	Filter / Slit Grating Name	Exposure Time (s)	Spectral Dispersion ($\text{\AA} \text{ pix}^{-1}$)	Wavelength Range (\AA)	Spatial Scale ($'' \text{ pix}^{-1}$)	Position Angle (deg)	Spatial Offset ($''$)
WFC3	12212	IBGU11BSQ	2011 Jul 07	F502N ...	1554	...	4963-5059	0.039
WFC3	12212	IBGU11BXQ	2011 Jul 07	F547M ...	779	...	5039-5909	0.039
STIS	8253	O5G402010	2000 Apr 15	G430M A	1796	0.28	4818-5104	0.051	89.85	0.05 S
STIS	8253	O5G402010	2000 Apr 15	G430M B	600	0.28	4818-5104	0.051	88.85	0.20 N

NOTE—A summary of the *HST* observations used in this study. The columns list the (1) *HST* Instrument, (2) Program ID, (3) Observation ID, (4) observation date, (5) filter (imaging) or grating (spectra), (6) assigned labels (names) for the two long slits, (7) total exposure time for each data set, (8) spectral dispersion of the long slit grating, (9) wavelength range (for spectra) or bandpass (for imaging), (10) spatial scale of the image/spectra, (11) PA of the STIS slits, (12) their spatial offsets from nucleus. The values in column (8)-(10) were obtained from their respective instrument handbooks (Dressel 2012; Riley 2017) where the exact STIS spatial scale is given as $0.05078'' \text{ pix}^{-1}$.

The slit PAs on the host galaxy are shown in Figures 1 and 2.

The DIS uses a dichroic element to split light into blue and red channels, allowing simultaneous measurements in the $H\beta$ and $H\alpha$ regions of the spectrum. For this study, we used high dispersion gratings B1200 (blue) and R1200 (red) with a resolving power $R \approx 4000 - 5500$. Similar to *HST*, we used the DIS blue spectra that contain strong [O III] lines and DIS red spectra that contain the $H\alpha$ and [N II] lines to measure kinematics of the circumnuclear and extended ionized gas. The spatial scales of the blue and red channels are $0''.42 \text{ pixel}^{-1}$ and $0''.40 \text{ pixel}^{-1}$, respectively. APO DIS provides a lower angular contrast than *HST* but offers larger spatial coverage that enables us to probe the rotation and possible extended outflow signatures in the host galaxy.

We obtained four long-slit observations corresponding to PAs of 98° , 188° , 143° , and 233° on the same night. We reduced the observed raw data to the two dimensional spectral images using a standard IRAF routine (Tody 1986, 1993), which involves primary calibrations such as bias subtraction, flat-field correction, cosmic ray removal with the IRAF task, LA Cosmic (van Dokkum 2001) and combining multiple exposures. We used the arc lamp images that were taken before every science exposure for the wavelength calibrations. Standard star exposures were taken on the same night for flux calibration (Oke 1990) and the data were corrected for atmospheric extinction using an APO extinction curve. Additional calibrations were performed using IDL to correct for tilt in the location of the spectrum in the cross-dispersion direction (Gnilka et al. 2020) and for sky line subtraction. Seeing for the observing night was measured by calculating the point-spread function (PSF) of the standard star. More

information about the instrument and observations are given in Table 2.

As discussed in Gnilka et al. (2020), the DIS experienced scattered light due to a contamination from condensation in the latter years of its operation. The instrument was serviced periodically for optical correction. We characterized the impact of the scattered light in our data by measuring the emission lines from the standard stars observed on the same nights. Strong broad wings or “halos” around the emission lines were seen in the observations after 2017 September 19. Fortunately, NGC 4051 was observed in the beginning of 2017 after an upgrade to the instrument. The blue channel shows no sign of scattered light in the spectral image, which provides us the best measurements of spectral lines such as [O III] and $H\beta$ for our kinematics analysis. However, we found faint scattered light close to the nucleus in the red channel ($H\alpha$ region) from the bright central NLR. Therefore, the spectra from $3''$ to $15''$ on both sides of the nucleus were slightly corrupted, which made it more difficult to separate the kinematic components of the $H\alpha + [\text{N II}]$ lines. We focused on the [O III] lines from the blue channel to measure the ionized gas kinematics and outflow structure in those regions. The spectra extracted for the extended part of the galaxy were unaffected and show strong narrow $H\alpha$ emission lines, which we use to measure the rotational kinematics of the host galaxy.

We also observed NGC 4051 with the Astrophysical Research Consortium Telescope Imaging Camera (ARCTIC) on the 3.5m telescope using its broadband Johnson Cousins B, V, and R filters (wavelength range is given in Table 2) to increase the spatial coverage and compare with the spectroscopic observations. ARCTIC has a field of view of $7.85' \times 7.85'$. The image was taken with 2×2 binning, which gives a plate scale of $0.228'' \text{ pixel}^{-1}$.

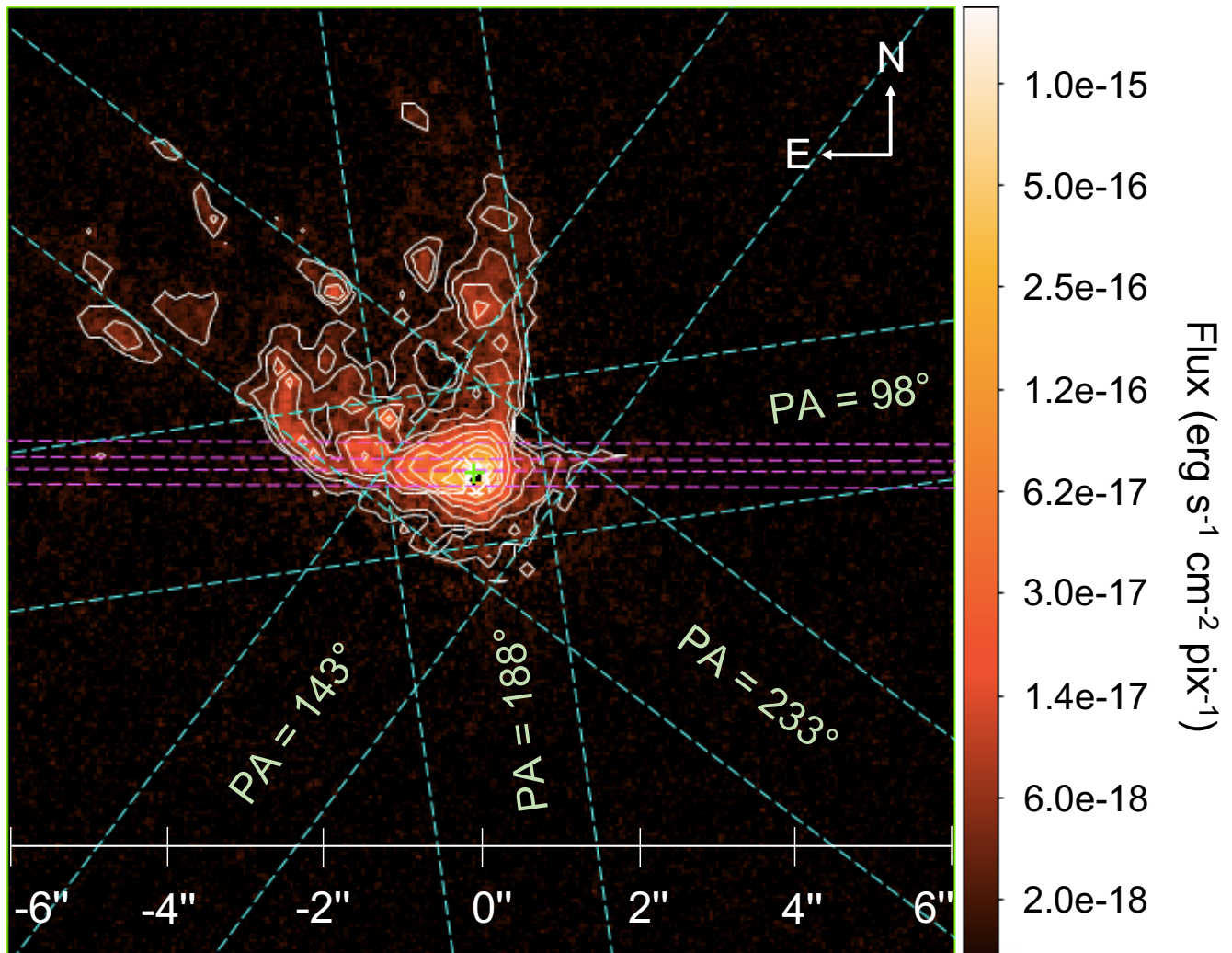


Figure 2. A $12'' \times 12''$ continuum-subtracted [O III] image of NGC 4051 using WFPC3 camera on *HST*. The APO (cyan) and STIS (magenta) slits are overlaid, with the APO PA labeled. The PA for both STIS slits is 89.8° . The flux contours are generated at 3σ above the background and increase in powers of $2 \times 3\sigma$ for each inner contour. The color bar on the right shows the flux variation in the units of $\text{erg s}^{-1} \text{cm}^{-2} \text{pix}^{-1}$. The standard deviation (σ) was calculated from a fraction of the background image outside the galaxy. The green cross marks the continuum centroid, associated with the highest flux position in the F547M continuum image. The dark spots are saturated pixels in F502N image due to the bright central point source. The STIS slits “A” and “B” are $0''.05$ south and $0''.2$ north of the nucleus, respectively.

The raw images were corrected for darks, bias and flat-fields using an open source automatic reduction pipeline named Acronym, which was developed at APO to reduce ARCTIC images (Weisenburger et al. 2017). We then combined the different exposures using the task IM-COMBINE in IRAF for each bandpass. A $400'' \times 400''$ RGB-composite image is shown in Figure 3, with the APO DIS long slit locations overlaid.

2.3. Slit Placements

Figure 2 shows a strong bright core of [O III] emission around the Seyfert 1 nucleus and additional emission along the walls of a cone-like structure extending to a

projected distance of $\sim 6''$ in the NE. Assuming this is part of a bicone, the SW cone is hidden by dust in the host galaxy as described by Fischer et al. (2013). The STIS slit positions capture portions of the walls of the cone. The APO DIS slits overlap at the nucleus. The APO slits at $\text{PA} = 233^\circ$ & 188° capture the east and north walls of the cone, albeit at low spatial resolution, while the slit at $\text{PA} = 98^\circ$ lies closest to and encompasses the STIS G430M slits in the regions of interest. The slit at $\text{PA} = 143^\circ$ is close to the projected major axis of the host galaxy, as shown in Figures 1 and 3. All of the APO slits cross areas of strong star formation in the spiral arms.

Table 2. ARC 3.5m Telescope Observations of NGC 4051 at APO

Instrument Name	Date (UT)	Filter / Grating	Exposure Time (s)	Spectral Dispersion (\AA pix^{-1})	Wavelength Range (\AA)	Spatial Scale ($'' \text{pix}^{-1}$)	Position Angle (deg)	Mean Air Mass	Mean Seeing ($''$)
ARCTIC	2020 Mar 23	J-C B	190	...	3400-6000	0.228	...	1.12	1.80
ARCTIC	2020 Mar 23	J-C V	80	...	4500-7000	0.228	...	1.16	1.80
ARCTIC	2020 Mar 23	J-C R	30	...	5400-10000	0.228	...	1.18	1.80
DIS	2017 Feb 27	B1200	2700	0.62	4373-5633	0.42	98	1.02	2.27
DIS	2017 Feb 27	R1200*	2700	0.58	6098-7283	0.40	98	1.02	2.24
DIS	2017 Feb 27	B1200	2700	0.62	4373-5633	0.42	143	1.07	2.27
DIS	2017 Feb 27	R1200*	2700	0.58	6098-7283	0.40	143	1.07	2.24
DIS	2017 Feb 27	B1200	2700	0.62	4373-5633	0.42	188	1.15	1.97
DIS	2017 Feb 27	R1200*	2700	0.58	6098-7283	0.40	188	1.15	1.68
DIS	2017 Feb 27	B1200	1800	0.62	4373-5633	0.42	233	1.26	1.97
DIS	2017 Feb 27	R1200*	1800	0.58	6099-7185	0.40	233	1.26	1.68

NOTE—A summary of the ground-based imaging and spectroscopy used in this study. The columns list (1) the APO instruments, (2) the observations dates, (3) filters (for imaging)/ gratings (for spectra) used, (4) the total exposure times for each data set, (5) spectral dispersion (6) wavelength range (for spectra) or bandpass (for imaging), (7) spatial scales of the images/spectra, (8) PAs for the long slits, (9) mean air mass and (10) mean seeing for the nights of observations. *Affected by the instrument scattered light.

3. ANALYSIS

3.1. Spectral Fitting in the [O III] region

We fit the [O III] $\lambda\lambda 4959, 5007$ lines in the *HST* STIS G430M and APO DIS blue channel spectra with multi-component Gaussian profiles. To fit Gaussians to emission lines along the slits at each position, we used a fitting routine, which employs a multimodal nested sampling algorithm called MultiNest (Feroz & Hobson 2008; Feroz et al. 2009, 2019; Buchner et al. 2014). The algorithm uses Bayesian statistics to determine the significant number of components that best fit the emission lines with the least complexity. The Gaussian fits output the wavelength centroid, width and peak flux of each component, which are used to calculate the mean velocity, FWHM and total flux of the ionized gas clouds as shown in Figure 4.

Although the emission lines are often asymmetric and not exactly Gaussian (Heckman et al. 1981; Veilleux 1991), employing a Gaussian model provides the simplest and most efficient method to decompose the line profile into different kinematic components, which are often seen as distinct bumps or even multiple peaks in the profiles. A detailed description of the Gaussian fitting routine can be found in the Appendix of Fischer et al. (2017). Our group has previously employed this technique (Revalski et al. 2018b; Fischer et al. 2018; Gnilka et al.

2020; Revalski et al. 2021) to study the gas kinematics in various AGN.

To achieve the best results, we fit the [O III] $\lambda\lambda 4959, 5007$ lines along with the $H\beta$ $\lambda 4861$ line and selected the adjacent regions on either side as continuum points, as shown in Figure 4. We fixed the relative height ratios of $\lambda 5007$ and $\lambda 4959$ to 3.01 and their wavelength difference to 47.9 \AA in the rest frame of the source (Osterbrock & Ferland 2006). We also set a wavelength difference for [O III] $\lambda 5007$ and $H\beta$ $\lambda 4861$ to 145.515 \AA for the narrow emission lines. The mean velocity and velocity widths (FWHM) of each component for both $H\beta$ and [O III] emission lines were fixed under the assumption that both of these lines originated from the same cloud. We restricted the width of the narrow component to vary above a minimum value associated with the spectral resolution (FWHM of the line-spread function) of the instrument. We also found contributions from an unresolved broad line region (BLR) and an intermediate line region (ILR) component associated with the nucleus. We limited the velocity widths of NLR emission to accommodate these two broad/intermediate components. See section §3.2 for more details.

The peak flux for all the components was allowed to vary from 3σ above the background noise level up to the maximum height of the emission line, with the standard deviation (σ) calculated from the average flux measured

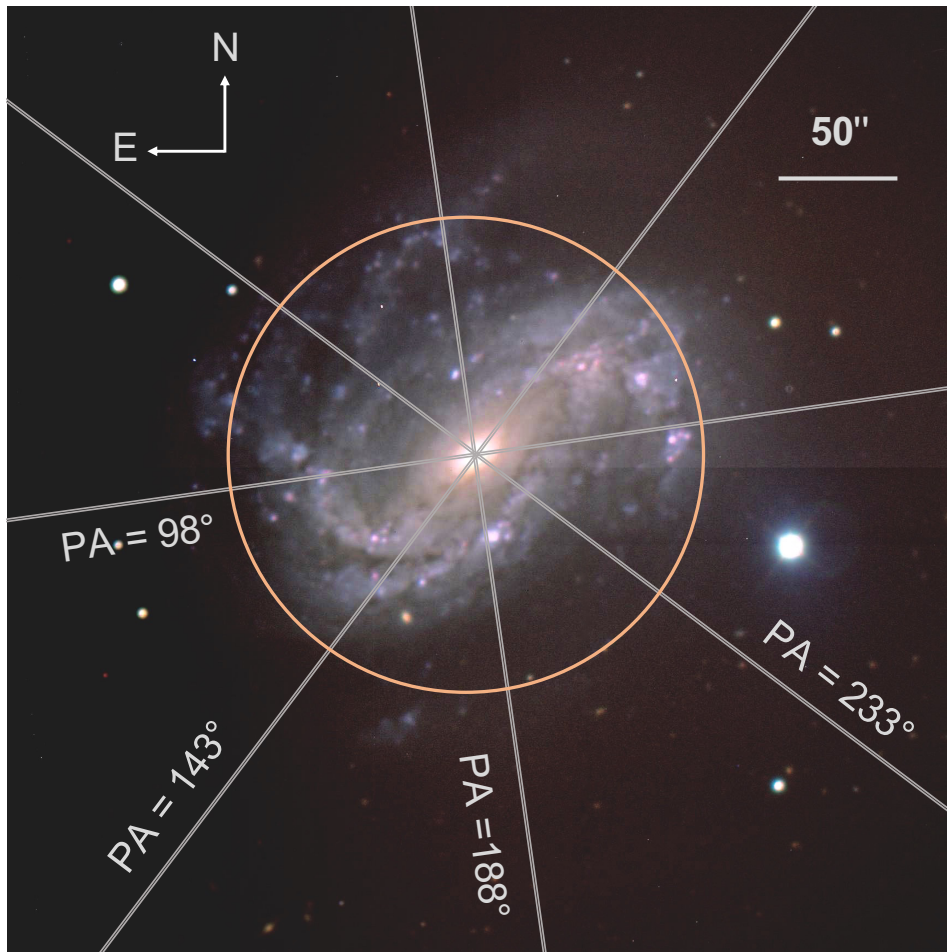


Figure 3. A $400'' \times 400''$ RGB-composite image of NGC 4051 obtained with ARCTIC on APO’s 3.5m Telescope. The four DIS slits are shown as grey lines and the circle with a $100''$ radius corresponds to the extent of $H\alpha$ velocities in Figure 10 and 11.

in the continuum regions free of any strong emission or absorption features.

3.2. Fitting the Broad and Intermediate Components

NGC 4051 is a narrow-line Seyfert 1 galaxy, which means the BLR emission lines such as $H\beta$ $\lambda 4861$ are relatively narrow compared to most Seyfert 1 galaxies, but still broader than the lines from the NLR. Therefore, we find little contamination of broad $H\beta$ towards the [O III] emission lines. Nevertheless, it is important to identify the contribution from broad $H\beta$ to separate it from the NLR components while fitting both [O III] and $H\beta$ simultaneously. The $H\beta$ BLR component was fit well by a single Gaussian unlike more complicated profiles often seen in normal Seyfert 1s (Marziani et al. 2009; Park et al. 2012; Barth et al. 2015). We measured the centroid and width of the broad component using a Gaussian fit to the $H\beta$ line at the nucleus. The wavelength centroid was found close to the systemic velocity of the galaxy and width of the broad emission line was measured as $\text{FWHM} = 2800 \text{ km s}^{-1}$. We fixed the centroid and width

of the broad $H\beta$ line as we moved the spectral fits along the slit. The flux of the broad component decreases smoothly with distance from the nucleus, as expected from the PSF of an unresolved source (the BLR).

In addition to the narrow emission lines and the broad $H\beta$ component, we detected a component with an intermediate width and density from an “intermediate line region”, which has been claimed in a number of other AGN (Crenshaw & Peterson 1986; Crenshaw & Kraemer 2007; Mullaney & Ward 2008; Crenshaw et al. 2009; Zhu et al. 2009; Adhikari et al. 2016), and specifically for NGC 4051 in He II and $H\beta$ emission lines (Kraemer et al. 2012; Yang et al. 2013). The intermediate component was found by noticing that the previous fits to the narrow $H\beta$ and [O III] lines near the nucleus in the APO spectra yielded a relatively “broad” ($\text{FWHM} \approx 1000 \text{ km s}^{-1}$) component with an unusually small [O III]/ $H\beta$ flux ratio (≈ 0.55), indicating significant collisional de-excitation of the level that gives rise to the [O III] $\lambda\lambda 4959, 5007$ lines at a critical density of $n_e = 6.8 \times 10^5 \text{ cm}^{-3}$ (Osterbrock & Ferland 2006). The intermediate component

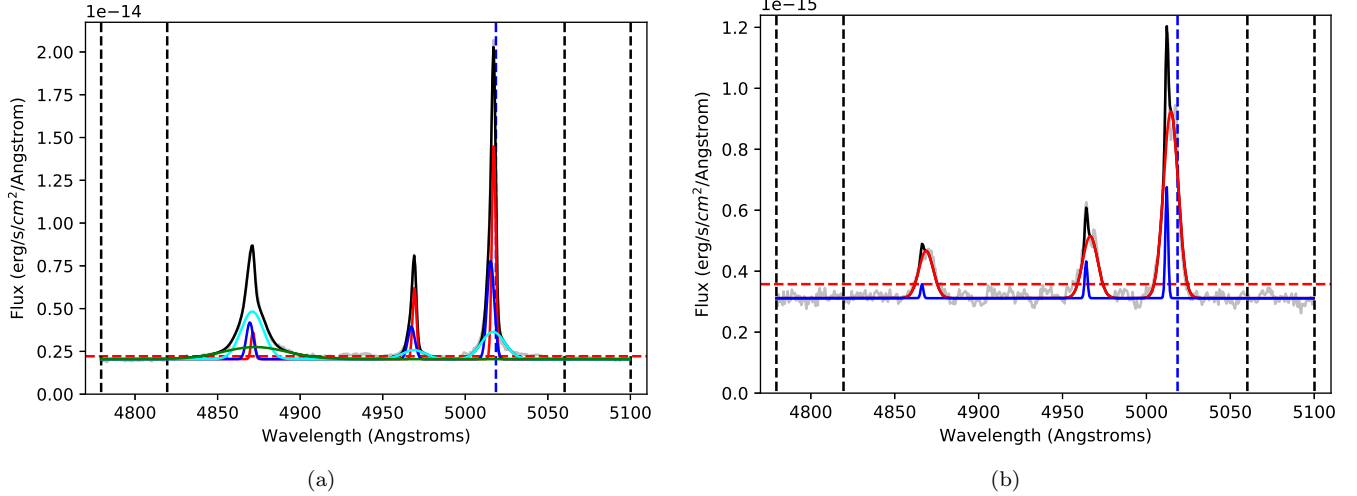


Figure 4. Examples of $H\beta$ $\lambda 4861$ and $[O III] \lambda\lambda 5007/4959$ emission lines fits with multi-Gaussian components for APO slit PA 188° . The observed data is shown in gray and the total flux with the multiple Gaussian fits is shown with a black solid line. (a) Spectral lines extracted at the nucleus and fit with two narrow components (red and blue) as well as a broad $H\beta$ component (dark green) and an intermediate broad component (cyan), which is present in both the $H\beta$ and $[O III]$ lines. Panel (b) shows a spectrum extracted at $2.5''$ to the north, which only contains two narrow components and a double-peaked profile. The vertical dashed black lines are the defined continuum regions, while the horizontal dashed red line represents the flux level at 3σ over the noise. The vertical blue dashed line close to $[O III]$ corresponds to the redshift of the galaxy.

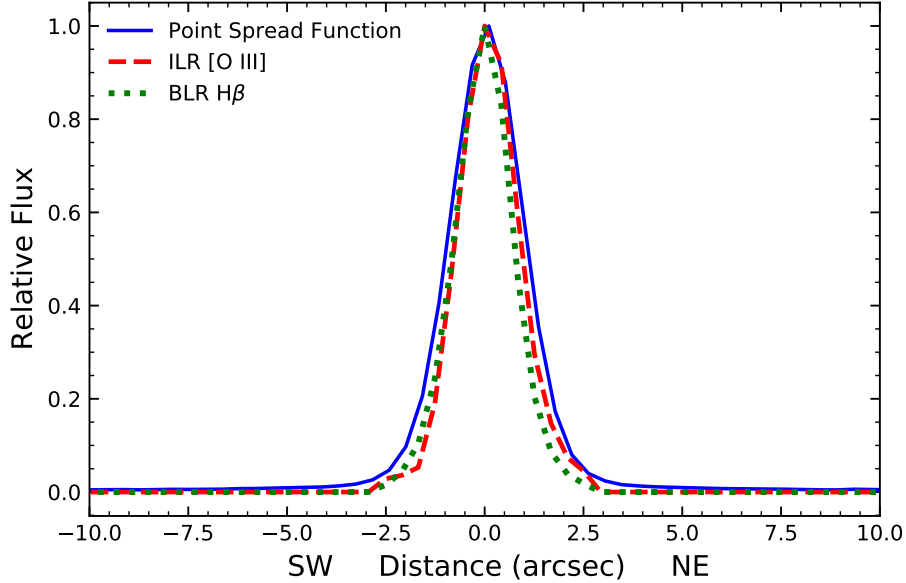


Figure 5. Normalized brightness profiles along the APO DIS slit giving the PSF from a standard star (solid blue line), the ILR component as seen in $[O III]$ (dashed red line), and the BLR $H\beta$ emission (dotted green line), demonstrating that the ILR and BLR are unresolved in the APO DIS slit. The slightly broader PSF of the standard star likely indicates slightly different seeing at the time and location of its observation.

is blueshifted from the host galaxy plane with a radial velocity centroid of $= -110 \pm 15 \text{ km s}^{-1}$ and has $\text{FWHM} = 1010 \pm 70 \text{ km s}^{-1}$, which is within the uncertainties of the intermediate $H\beta$ $\text{FWHM} = 1137 \pm 178 \text{ km s}^{-1}$ as measured by Yang et al. (2013).

Similar to the broad $H\beta$ component, the intermediate component is unresolved in both the STIS and APO spectra, consistent with a location close to the SMBH. Therefore, in the revised spectral fits, we restricted the FWHM of the narrow components to be $\leq 900 \text{ km s}^{-1}$.

At the same time, we fixed the velocity centroid and velocity width of the broad and intermediate components while allowing the fluxes to change along the slit.

A comparison of the radial extents of the broad $H\beta$ and intermediate [O III] components with the PSF, as calculated from standard star brightness profiles, is shown in Figure 5. Due to the simultaneous fit, both $H\beta$ and [O III] ILR components have the same velocity and width as well as radial extent. On the other hand, unlike broad $H\beta$, the [O III] does not have a BLR component and therefore does not affect the BLR brightness profile in Figure 5. Figure 5 indicates that broad $H\beta$ and intermediate ([O III] and $H\beta$) components are unresolved within the spatial resolution of the APO spectra, and appear in the extended emission due to seeing (see Table 2). The broad $H\beta$ and intermediate $H\beta$ & [O III] components were also detected in the STIS spectra as point sources, which limits the projected size of the ILR to $\leq 0''.1$ (~ 8 pc). We will discuss the ILR size calculations in section §5.2.

An example of emission line fitting is shown in Figure 4 for spectra obtained with one of the APO DIS long slits. The double peaked [O III] emission line seen in Figure 4b is similar to those in space/ground based spectra of several Seyfert galaxies and can be attributed to the asymmetric distribution of ionized gas in NLR and/or to distinct contributions from the rotating disk and outflowing gas (Rosario et al. 2010; Fischer et al. 2011; Shen et al. 2011; Wylezalek et al. 2020).

3.3. Gaussian Fitting to Other Emission Lines

To measure the line ratios for ionization diagnosis (§4.3) for the APO observations, we fit emission lines $H\beta$ $\lambda 4861$; $H\alpha$ $\lambda 6563$; [N II] $\lambda\lambda 6548, 6583$; and [S II] $\lambda\lambda 6716, 6731$ by using the multi-component fits of the [O III] lines as a template. The procedure, described in detail in Revalski et al. (2018a,b, 2021), fixes the positions and widths of the emission-line components based on the [O III] kinematics, and allows the fluxes to vary, subject to atomic constraints on fixed ratios such as those of the [O III] and [N II] doublets. An example of the fits to the emission lines in the red APO spectra is shown in Figure 6. This analysis was not done for the *HST* STIS spectra, because there are no G750M or G750L spectra available for the same PA as the G430M spectra to compare the line flux of the above lines at the same location in the NLR¹.

The DIS blue and red channel spectra permits us to simultaneously observe all of these lines at each location,

which allowed us to generate Baldwin-Phillips-Terlevich (BPT) diagrams (Baldwin et al. 1981; Veilleux & Osterbrock 1987; Kewley et al. 2001; Kauffmann et al. 2003; Kewley et al. 2006) and determine the ionization mechanism of the gas in the NLR-ENLR (see section §4.3). To fit the $H\alpha$ line from the red channel spectra, we used [O III] and $H\beta$ to obtain the wavelength centroid, width, and number of narrow components as well as the broad and intermediate $H\alpha$ component along the slit as identified in broad and intermediate $H\beta$. The wavelength centroid and width of each line were scaled to the corresponding emission line under the assumption that emission produced from the same cloud will provide the same mean velocity and dispersion. We also fit $H\alpha$ independently for the spectra extracted inside $3''$ and outside $15''$ radii of the nucleus for the DIS red channel for the reasons described in the next section. Fits in the inner regions help to compare [O III] kinematics with $H\alpha$ in the NLR and at larger radii, they provide the rotational kinematics of the host galaxy.

3.4. Effects of the APO Point-Spread Function

As shown in Figure 2, the APO slits are larger compared to the size of the NLR, and the bright NLR core convolved with the seeing PSF can affect kinematic measurements of the emission lines beyond $\sim 2''$ ². We simulated this effect by combining the STIS spectral images at PA = 89.8° and degrading them to the spectral and spatial resolutions of the APO DIS blue spectral image at PA = 98° . We accomplished the latter by convolving the combined STIS spectra with Gaussians representing the line-spread function of APO in the dispersion direction (FWHM $\approx 1.2 \text{ \AA}$) and the PSF seeing at the time of the APO observations (FWHM $\approx 2''.2$) in the cross-dispersion direction, and binning the convolved spectra to the spectral and spatial scales of APO DIS.

Figure 7a presents a brightness profile of the [O III] emission along the combined STIS slits after continuum subtraction, which shows the bright central core of emission and the structure due to distinct [O III] knots to the east of the core (see Figure 2). The convolution erases this spatial structure and extends the brightness profile outward to match that of the [O III] emission from the APO spectrum, as expected. The APO brightness profile has enhanced wings compared to that of the convolved STIS spectrum, likely due to the inclusion of more NLR emission-line knots in the APO DIS slit at PA = 98° , as shown in Figure 2. To account for this effect in the

¹ The G750M observations in the *HST* archives are short and lie outside of the nominal bicone at PA = 133° .

² The APO PSF also blurs the spatial locations of the kinematic components within $\sim 2''$, but we have these inner regions partially covered with *HST* STIS slits.

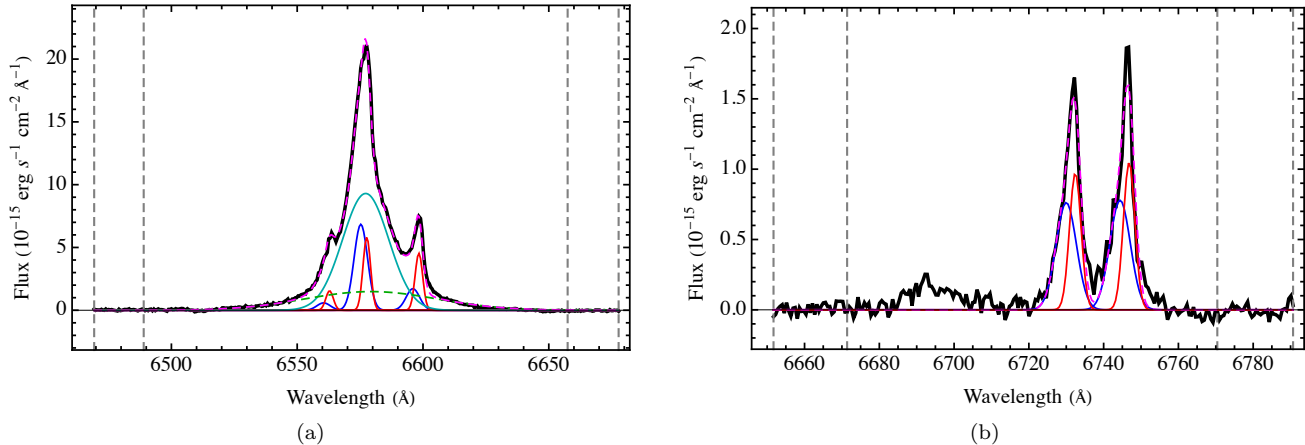


Figure 6. Examples of (a) H α λ 6563 + [N II] λ 6548,6583 and (b) [S II] λ 6716,6731 emission line fits with multi-Gaussian components for APO slit PA 188 $^\circ$ at the nucleus. The velocity centroid and width of each component are fixed for all emission lines as determined from the [O III] λ 4959,5007 fits. The observed spectra are plotted in solid black. The NLR emission Gaussian fits are shown in blue and red for wider and narrower kinematic components. The broad (dashed) green and cyan curves in (a) show the broad line region and intermediate line region H α emission, respectively. The sum of all components is given in dashed magenta.

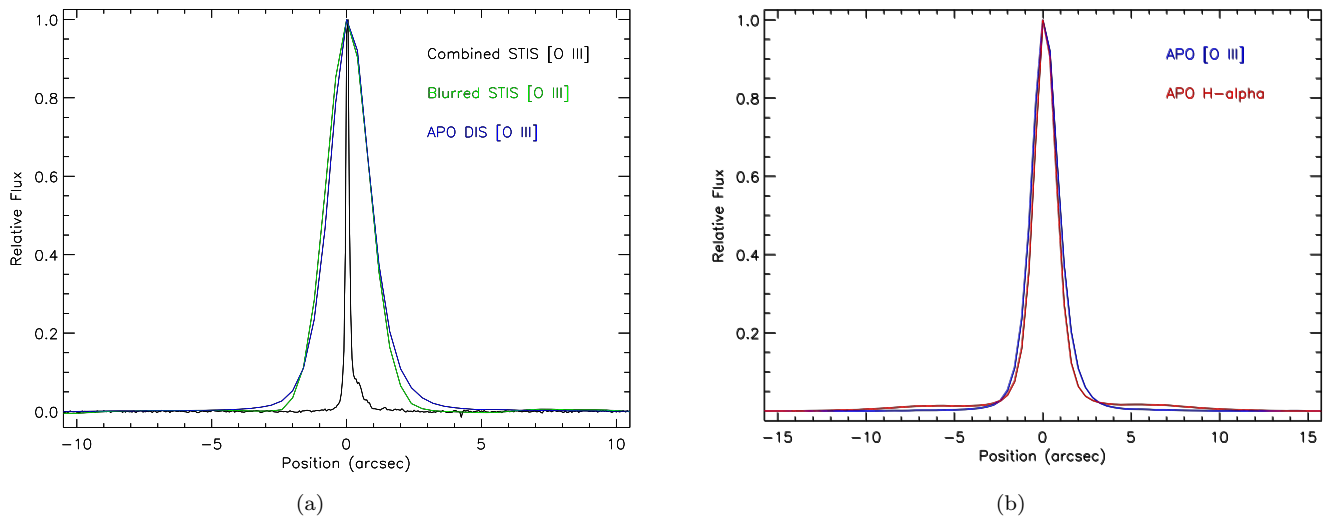


Figure 7. (a) A test to identify the effects of the PSF in the APO observations. We compare the [O III] brightness profiles from the combined STIS spectra, APO slit, and SITS spectra convolved with the APO PSF. (b) A comparison of the brightness profiles of the [O III] emission (blue channel) and H α emission (red channel) along the slit. The enhanced emission in the wings of the H α profile at 3'' - 15'' on both sides of the nucleus.

APO spectra, we identify kinematic components in the extended emission that match those in the NLR core in velocity and width and are consistent with a continuation of the PSF, and exclude those from further consideration.

In the right panel of Figure 7, we show the brightness profile of the H α emission from the red APO channel compared to that of [O III] from the blue channel. The H α profile shows enhanced emission from 3'' to 15'' at the level of 1 - 2% of the peak flux, due to the scattering problem in the red channel discussed earlier, which is why

we exclude the measurements of H α and other emission lines from the red channel in this region.

4. RESULTS

4.1. Ionized Gas Kinematics

Figure 8 shows the kinematic and flux distributions of [O III] ionized gas up to 10'' (\sim 800 pc) from the central SMBH in NGC 4051, from both *HST* and APO long slit observations. The first column corresponds to *HST* STIS G430M slits A and B. Slit A (offset 0'05

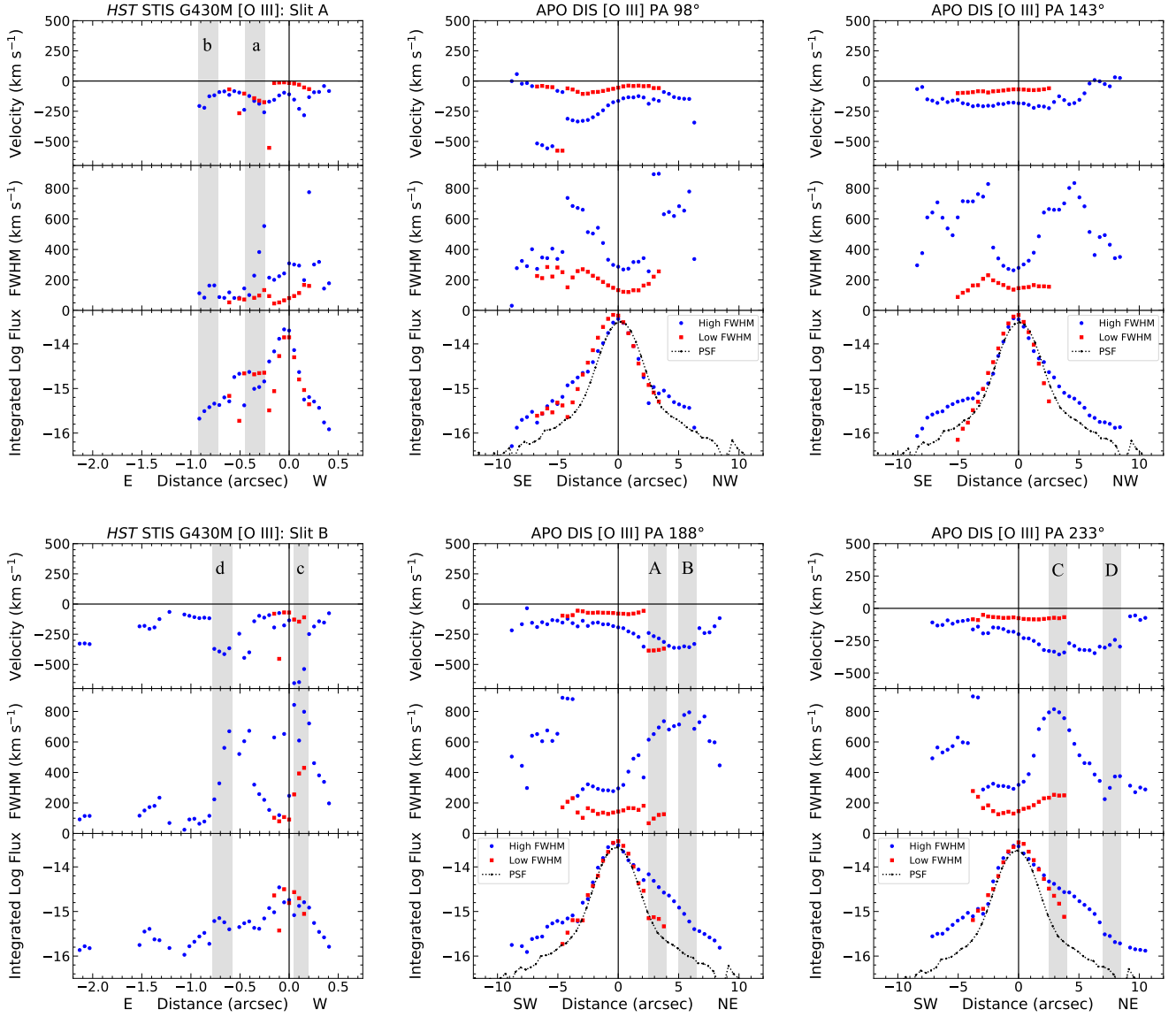


Figure 8. The [O III] ionized gas kinematics for NGC 4051. The left column presents the observed kinematics inside the two *HST* STIS G430M slits labeled as A (offset $-0.05''$) and B (offset $+0.20''$) at PA 89° . The second and third columns contain the kinematics of the four APO DIS slits (PAs 98° , 143° , 188° , 233°). The positions of the *HST* and APO slits can be seen in Figure 2. The top panels of each figure shows the radial velocity distribution of the [O III] emitting gas along the slits for the two narrow components. The middle panels show the FWHM distribution of these components and the bottom panels map the radial variation in the integrated flux in logarithm ($\text{erg s}^{-1} \text{cm}^{-2}$) for each line component. Because the APO slit width ($2''$) is 10 times wider than the G430M slit ($0.2''$), it captures the integrated emission at larger distances (up to $\sim 10''$) that are too faint (below $S/N < 3$) to be detected with the narrow G430M slits. The two NLR components are shown in blue circles (high FWHM) and red squares (low FWHM). The black dotted line in the bottom panel outlines the spread the PSF of the instruments as determined by the brightness profile of the standard star observation on the same night. The velocities are shown after subtracting off the systemic velocity of the galaxy. The FWHM values have been corrected to intrinsic values by subtracting the line-spread function in quadrature. The vertical lines at $0''$ correspond to the continuum centroid of each slit. The points inside the shaded regions of the two STIS slits and APO slits PAs 188° and 233° are selected as separate knots of outflow based on their clustering in flux and/or kinematics, and will be employed for radiation-gravity model in section §4.5.

to the south) is closer to the nucleus and encompasses higher flux clouds than slit B ($0''20$ to the north), which covers part of the outflow bicone up to a larger distance than slit A, although neither are fully along a bright

edge of the bicone. Our Bayesian algorithm does not fit emission lines below 3σ over the noise and therefore shows fewer velocity points than from the manual fitting analysis we performed previously (Fischer et al. 2013).

However, the overall kinematic structure is very similar to that presented in Fischer et al. (2013). The FWHM distribution shows most of the kinematics have FWHM $< 400 \text{ km s}^{-1}$ in slit A. The widths are larger on average for slit B, which is slightly farther from the nucleus. In general, the clumping together of points in velocity, FWHM, and flux indicates that STIS is resolving the individual knots of [O III] emission, some of which can be seen in Figure 2.

Nearly all of the radial velocities in the STIS observations are blueshifted or near zero compared to the systemic velocity of NGC 4051 (at zero in these plots). The emission is more extended in the east due to the relative orientations of the slits and cone, which can also be seen in Figure 2. We observe blueshifted velocities up to $\sim 500 \text{ km s}^{-1}$ inside $1''$ to the east for higher FWHM ($> 200 \text{ km s}^{-1}$) clouds. The [O III] line splitting as mentioned in Christopoulou et al. (1997) can be seen in the two velocity components separated by $\sim 150 \text{ km s}^{-1}$ at $\sim 0.5''$. With the exception of a few points, the narrow component is close to the systemic velocity of the host galaxy.

The morphology of the ionized gas in Figure 2 and its location mostly to the NE of the nucleus, together with the presence of mostly blueshifted radial velocities, suggests an outflowing bicone of ionized gas, where the SW, redshifted cone is likely hidden behind the host disk. In Fischer et al. (2013), the modelling of the outflow bicone was carried out using the kinematics from these two *HST* G430M slits. As seen from the [O III] image in Figure 2, the blueshifted cone is clearly visible and lies to much further extents than the G430M slits coverage, which is also comparable to that seen in the MERLIN Echelle Spectrograph (MES) [O III] image (Christopoulou et al. 1997) and [S III] observations with GEMINI GMOS/IFU (Barbosa et al. 2009).

To estimate the total extent of AGN ionized gas and the size of AGN driven outflows, we used the APO DIS spectra with wider slits that may detect the low flux emission. As seen from Figure 2, the four APO slits cover nearly all of the ionized “cone”. Similar to the G430M observations, we measured the velocities, FWHM and flux of the ionized gas by using Gaussian fits to the emission lines in these four slits as shown in the second and third column of Figure 8. The narrow [O III] emission lines can be fit with two kinematic components, except in more distant, fainter regions where one component is sufficient. We focus on the emission outside of that covered by STIS ($\gtrsim 2''$ from the nucleus) and kinematic components that are clearly not due to the wings of the PSF from the bright central [O III] knots (Figure 8).

The two NLR components are sorted by FWHM and color-coded as blue (high FWHM) and red (low FWHM). In most cases, the points with higher FWHM have higher velocity than the ones with lower FWHM except for a few positions when the narrower component corresponds to a higher velocity centroid. In a couple of instances, the high and low FWHM components have switched locations in the velocity plots, such as those at $-5''$ in the 98° slit, which is likely due to their relatively similar FWHM derived from the Gaussian fitting routine. Although a large majority of the APO NLR points have FWHM less than the maximum allowed width (900 km s^{-1}), a few points reach the maximum FWHM. Those at $+3''$ in the 98° slit may be due to contamination from the ILR component, whereas the points at $-4''$ are likely real due to their high fluxes above the ILR PSF. We detect significant jumps in velocity and FWHM curves in both STIS and APO observations (Figure 8). This is because we are detecting separate ionized gas knots (as shown in Figure 1) that have their own peculiar velocities and FWHMs, and therefore, the noticeable jumps between two adjacent points are due to transitions between these knots. The clumping of points together in the APO data is due to a convolution of the finite extent of the clouds with the seeing.

The APO observations at PA = 98° cover the emitting gas in the two *HST* STIS G430M slits but with lower spatial resolution. In this and all other slits we see a bright, narrow, slightly blueshifted component at $\sim -70 \text{ km s}^{-1}$ extending to $\pm 5''$ that is likely due to the PSF from the bright core. There is a high FWHM blueshifted component at $\sim -300 \text{ km s}^{-1}$ from $2'' - 4''$ in the east that is similar to the STIS blueshifted emission closer in and clearly not due to the PSF. In addition, we observe high blueshifted velocities of -550 km s^{-1} towards the east between $5''$ and $7''$, just outside of the nominal cone, which extends the outflows beyond those seen in the STIS data. The APO slits at PA = 188° and 233° align along the two edges of the cone and encompass the majority of the [O III] emission. We see line of sight velocities up to $\sim -400 \text{ km s}^{-1}$, extending the detection of outflows up to a projected distance of $\sim 8''$ ($\sim 640 \text{ pc}$) in the NE. At PA = 143° , which lies close to the major axis of the host galaxy, we continue to detect two components of blueshifted emission, although no velocities exceed -250 km s^{-1} . We built an outflow bicone model based on kinematics from the slits at PA = 188° and 233° in section §4.4.

Our observed velocities are in agreement with those of Christopoulou et al. (1997), Barbosa et al. (2009), and Fischer et al. (2013) at smaller radii. Similar to the STIS spectra, the narrowest component close to the nucleus

is near systemic velocity with a slight blueshift of only $\sim -70 \text{ km s}^{-1}$. It is ambiguous as to whether this is part of the host galaxy rotation or part of outflows close to the plane of the galaxy. The wider component (blue points) clearly traces blueshifted outflows at distances from $2''$ to $8''$ with high velocity widths ($\text{FWHM} > 400 \text{ km s}^{-1}$). However the FWHM of emission in the slit along PA $233''$ starts to fall after $5''$ while still moving with velocities $\sim -400 \text{ km s}^{-1}$. A few points around $10''$ – $11''$ in the NE are close to zero radial velocity but with a rather large FWHM of $\sim 200 \text{ km s}^{-1}$, suggesting a limit to the outflows and transition to rotation.

4.2. Comparison with Rotation

To separate a possible rotational component from the outflow component of the ionized gas, we need to compare the observed kinematics with a rotational curve obtained at the same radii. Riffel et al. (2008) present the stellar kinematics (GEMINI/NIFS K-band observations) within $3''$ of the nucleus with turnover radius at $\sim 1''$. The amplitude of the stellar rotation curve varies from -40 km s^{-1} to $+40 \text{ km s}^{-1}$ from SE to NW with a major axis given at 120° , close to the photometric axis of the large scale disk at PA = 130° (Kaneko et al. 1997). Figure 9 shows a comparison between stellar and [O III] ionized gas kinematics within the NLR. We projected the stellar velocities (PA = 120°) to APO PAs of 98° and 143° to identify any gas clouds that are part of the host galaxy rotation and not radially driven outflows. From Figure 9, we don't see any APO points that are close to the stellar velocity curve. There are a few STIS points close to the nucleus that could be part of the rotation curve, although they do not show a distinct rotation pattern so they are ambiguous.

We derived the rotation curve for the host galaxy using the kinematics of extended ionized gas at distances $10''$ – $100''$. We calculated the mean velocities by fitting Gaussian profiles (see section §3.1) to relatively narrow ($\text{FWHM} \leq 150 \text{ km s}^{-1}$) [O III] and $\text{H}\alpha$ lines separately from spectra extracted at those distances for all four long slits. In all cases, the Gaussian fits required only one kinematic component.

We then compared our observed line of sight velocities with neutral hydrogen (HI) 21-cm observations (Verheijen & Sancisi 2001) and ionized gas ($\text{H}\alpha$) kinematics (Kaneko et al. (1997); Richards et al. (2016)). Figure 10 shows the APO [O III] and $\text{H}\alpha$ velocities along with HI and ionized gas velocity fields that were obtained from the corresponding papers. We projected these extracted values to the APO slit positions. The adopted major axis was given as 310° , 130° , and 311° and inclinations adopted were 49° , 37° , 44.6° by Verheijen &

Sancisi (2001); Kaneko et al. (1997) and Richards et al. (2016), respectively. Our kinematics are in excellent agreement with these previous works, particularly for PA 143° , which is close to the major axis of the galaxy. By comparing the large scale rotation curves to the velocities within $\pm 10''$ of the nucleus (dashed vertical boundaries in Figure 10), the points that lie above $\sim 100 \text{ km s}^{-1}$ are clearly part of the outflowing gas. We find no evidence for AGN driven outflow at distances greater than $\sim 10''$ ($\sim 800 \text{ pc}$) from the nucleus.

We also took an opportunity to model the host galaxy major axis and inclination using our observed (extended) gas kinematics. The modelling was performed with the publicly available Diskfit (Spekkens & Sellwood 2007; Sellwood & Spekkens 2015; Kuzio de Naray et al. 2012; Peters & Kuzio de Naray 2017) software package. Diskfit is generally used to fit simple symmetric models to disk galaxies using either photometric data or kinematic maps. We derived a rotation curve to NGC 4051 using APO DIS long slit kinematics. The extended (up to $\pm 100''$ from the nucleus) velocity maps for $\text{H}\alpha$ and [O III] ionized gas are shown in the top panel of Figure 11. The $\text{H}\alpha$ velocity fields are much stronger and extend to larger distances than [O III], which is ascribed to robust star formation (Bartunov et al. 1994; van Dyk et al. 1996; Anderson et al. 2012) that produces strong $\text{H}\alpha$ and $\text{H}\beta$ emission lines, but weaker [O III] at those distances.

We fit a simple rotational model to the host galaxy using extended $\text{H}\alpha$ velocities and assumed a circular motion of the disk. As discussed above, we were unable to claim any points in the inner $\pm 10''$ as part of the disk galaxy rotation with certainty, so it was not possible to model a rotation curve for the circumnuclear regions. To fit a rotation model to the extended galaxy, we removed the velocities from the inner $\pm 10''$. The modeled velocity field and residuals are shown in Figure 11 as the bottom two panels. The Diskfit model provides a host galaxy PA of 135 ± 2 and inclination of 43 ± 1 in degrees, within 5° and 2° of the values determined by Kaneko et al. (1997), respectively (see section §4.4). The systemic velocity was corrected from 0 km s^{-1} to 13 km s^{-1} , indicating the accuracy of our velocities when compared to the adopted systemic redshift from 21-cm observations.

4.3. Ionization Diagnostics of Observed Emission lines

To accurately identify the extents of AGN driven outflows and fit the best model to the outflow bicone, it is important to determine whether the observed gas is ionized by the AGN, star formation, or both, over a range of radial distances from the nucleus. To determine the source of ionization, we generated spatially resolved Baldwin-Phillips-Terlevich (BPT) diagrams (Baldwin

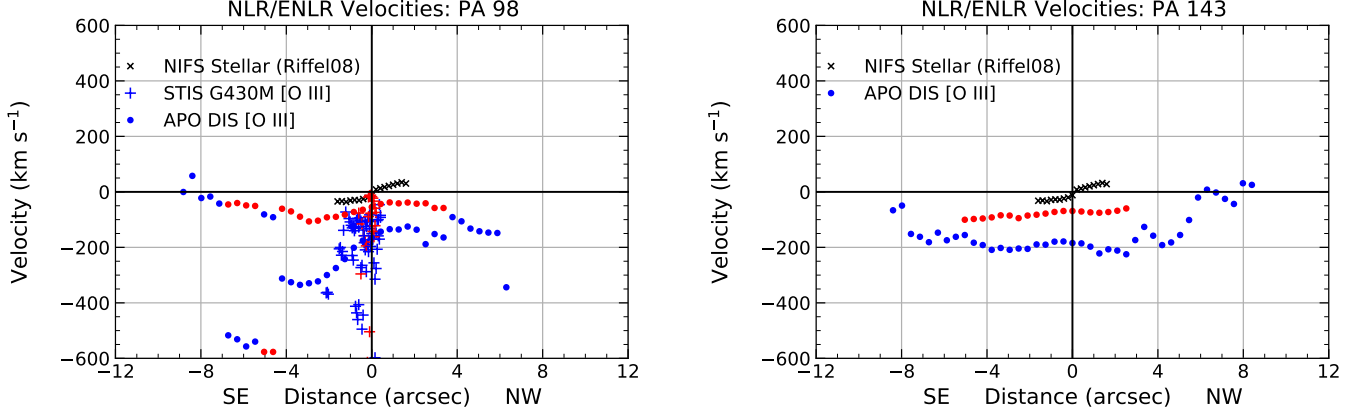


Figure 9. A comparison of stellar kinematics (black cross) from (Riffel et al. 2008) with [O III] ionized gas kinematics from STIS G430M (high to low FWHM in blue-red cross points) and APO DIS (high to low FWHM in blue-red dots) observations. NIFS stellar rotation curve is projected for the line of sight velocities onto APO PA = 98° and 143°. The observed STIS velocities for two parallel slits (PA 89.9°) are plotted along PA 98° as the wide APO slits (2'') covers the entire region inside both STIS slits. No STIS observation is available to compare the kinematics with the other APO slits at PA 143°, 188° and 233°.

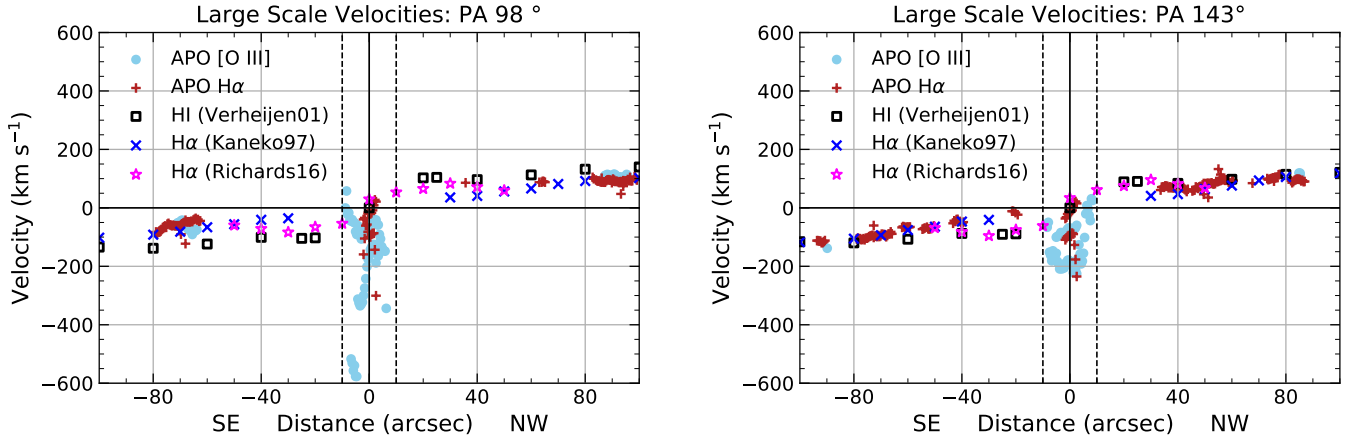


Figure 10. A comparison of the neutral (HI 21-cm) and ionized gas ([O III] and H α) kinematics for PAs = 98° and 143°. The APO [O III] and H α observations (this work) are compared with projected HI (Verheijen & Sancisi 2001) and H α (Kaneko et al. 1997; Richards et al. 2016) rotation curves within 100'' (~ 8 kpc) of the nucleus of NGC 4051. The dashed vertical lines give the extent of the NLR [O III] and H α emission detected by APO long slits.

et al. 1981; Veilleux & Osterbrock 1987) for the APO long slit observations. Two separate diagnostics were made using the demarcation lines defined by Kewley et al. (2001, 2006) and Kauffmann et al. (2003), as shown in Figure 12 for [O III]/H β versus [N II]/H α (first column) and [S II]/H α (middle column) line ratios. The line ratios were computed for each point in the spatially resolved kinematic components as discussed in section §4.1 (see Figure 8).

The BPT plots in Figure 12 show that for all four APO slits, the majority of the narrow components lie completely in the AGN ionized section, while a horizontal spread is noted for some of the wide kinematic compo-

nents specifically towards the SW and NW. This spread could be due to the uncertainties in Gaussian fitting of the blended H α + [N II] lines while isolating the broad and intermediate H α components near the nucleus.

Possible circumnuclear star formation in NGC 4051 has been claimed previously, using observations of dense molecular gas (Sani et al. 2012; Kohno et al. 2007) and weak polycyclic aromatic hydrocarbon (PAH) emissions (Rodríguez-Ardila & Viegas 2003; Sani et al. 2010) as close as 1'' – 2'' from the nucleus. This may explain the points near the AGN/H II composite line in the BPT diagrams. The dark red and white squares plotted inside the dashed box are points that are associated with the

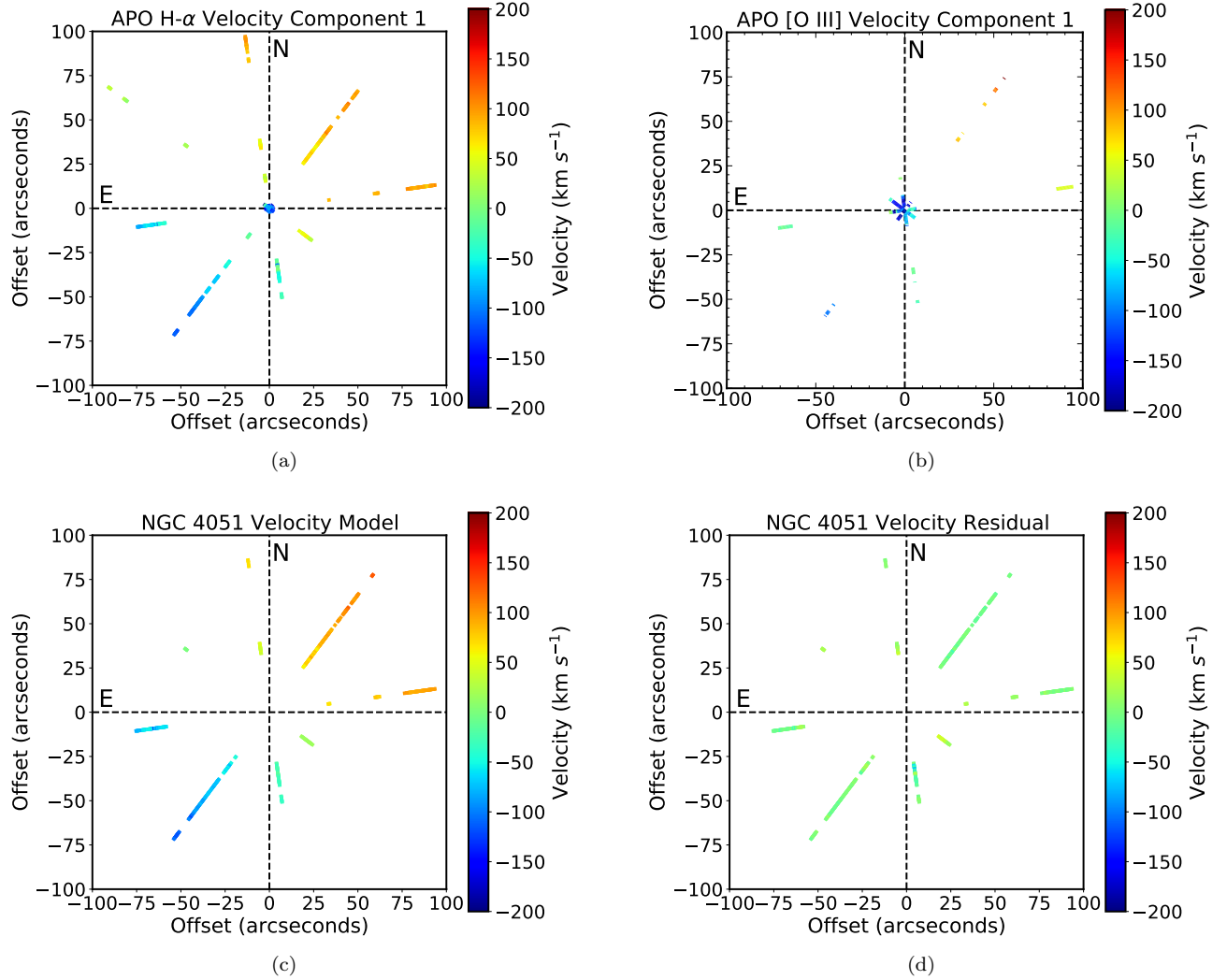


Figure 11. Figure (a) and (b) show a comparison of large scale $H\alpha$ and $[O III]$ kinematics in NGC 4051. A rotational velocity signature can be noticed in both emission lines although $H\alpha$ is more dominant and extended than $[O III]$. The extended $[O III]$ kinematics were too weak to generate sufficient number of data points to model the velocity fields. Therefore, we used $H\alpha$ kinematics to fit the circular (rotational) velocities of the host galaxy using the Diskfit software package. Figure (c) and (d) show the modeled and residual velocity maps derived by Diskfit.

emission lines measured between $20''$ to $100''$ from the center and include parts of the spiral arms, and hence show the large scale star formation in NGC 4051.

For our BPTs, we excluded the points at $3'' - 10''$ on both sides of the nucleus, due to the scattering observed at those parts in red channel spectra (see section §2.2), which includes the $[N II]$, $H\alpha$, and $[S II]$ lines. For those distances, we plotted the $[O III]/H\beta$ line ratio as a function of distance (see last column of Figure 12) using APO blue channel spectra, which is unaffected by instrument scattering. Although, the complimentary $[N II]$, $H\alpha$ and $[S II]$ lines are important to provide the best judgement for ionizing sources, in the absence of these lines, we rely upon the $[O III]/H\beta$ emission line

ratio alone. In Figure 12, the last column shows the spatial distribution of $[O III]/H\beta$ for four slits.

The points with $[O III]/H\beta \geq 3$ (shown as a horizontal dashed line at $\log(\frac{[O III]}{H\beta}) = 0.48$) show likely AGN ionization (Shuder & Osterbrock 1981) and points with lower values of $[O III]/H\beta$ are most likely starburst or composite regions. We notice a gradual increase in this ratio towards the north particularly in slit PAs 188° and 233° which contain the majority of the AGN ionization cone as seen in the $[O III]$ image in Figure 2. These regions also coincide with the high velocity clouds as seen in the APO kinematics in Figure 8. Points in the SE and SW below the dashed line, with $[O III]/H\beta = 1$ to 3, are consistent with a composite AGN/SF ionization as seen in the left and middle panels of Figure 12.

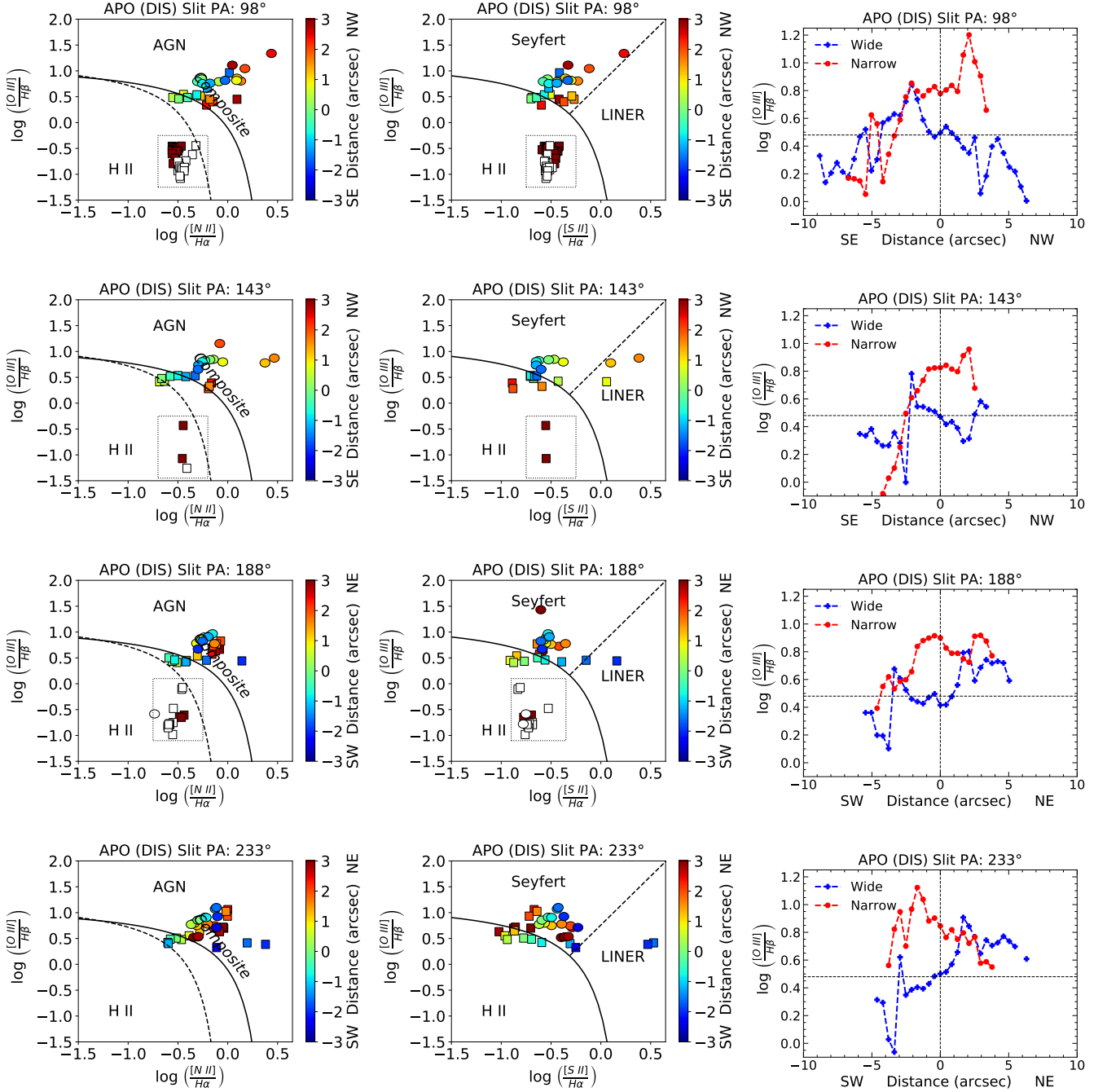


Figure 12. BPT ionization diagnostics using the APO DIS observations (PAs 98°, 143°, 188°, and 233°) for the two kinematic components. The first and second columns show the BPT diagrams using [O III] λ 5007, H β λ 4861, H α λ 6563, [N II] λ 6584, and [S II] λ 6716,6731 emission lines. The squares and circles represent the wide (higher FWHM) and narrow (lower FWHM) velocity components. The color of each point represent the distance from the nucleus as given in the colorbars on the right. H II regions correspond to star forming gas. The dark red and white squares inside the dashed rectangular boxes show the star forming regions at 20'' to 100'' to the north (red) and south (white) of the center, which lie in the spiral arms that can be matched with APO DIS slit positions on the color composite ARCTIC image in Figure 3. The third column shows the radial variation in [O III]/H β ratio for the wide (blue) and narrow (red) components. The horizontal dashed line corresponds to [O III]/H β = 3, which is an approximate discriminator between star-forming (below the line) and AGN (above the line) regions.

Thus, Figure 12 shows that the AGN either dominates or is a strong contributor to the ionization of gas to a

projected distance of $\sim 10''$ (~ 800 pc) from the nucleus, which also corresponds to the extent of the outflows. If

we use these two criteria (AGN ionization and evidence for outflows) to define the NLR, then we have not clearly detected an ENLR (AGN ionization plus rotation) in NGC 4051.

4.4. Outflow Model

In order to de-project the observed distances and radial velocities of the emission-line knots in the NLR of NGC 4051 and obtain their true distances and velocities, we need a kinematic model of the outflow. We presented a biconical outflow model of NGC 4051 based on the *HST* images and spectra alone in Fischer et al. (2013). The APO spectra, extending the [O III] kinematics to larger distances, and an enhanced version of the *HST* [O III] image, shown in Figure 2, allow us to revise the biconical outflow model. The enhanced image indicates a larger opening angle than originally thought and the APO spectra, which cover more of the projected bicone as shown in Figure 2, indicate that the outflows extend to larger distances than seen in the STIS spectra.

We therefore used the kinematic modeling code originally presented by Das et al. (2005) to match the new observational constraints. Consistent with the models of other AGN outflows in Fischer et al. (2013), the best model appears to be a symmetric bicone that is evacuated along its core, characterized by a minimum and maximum half-opening angle (HOA), and a simple velocity profile that increases linearly from zero at its center to a maximum velocity at a particular turnover radius, followed by a roughly linear decline to near zero (or systemic) at a maximum height along the bicone axis. The best fit comes from varying these parameters and the inclination of the bicone axis from the plane of the sky, which affects the amplitudes of blueshifts and redshifts on either projected side of the nucleus. Radial velocities extracted from the 3D kinematic model through a pseudo slit at the observed PA result in “envelopes” (due to the thickness of the bicone) that are compared to the observed radial velocities at that PA.

The parameters of the biconical outflow models were adjusted to provide a reasonable fit to the *HST* [O III] image (constraining the PA and maximum opening angle of the bicone) and the APO observed radial velocities obtained at the two PAs that lie along the edges of the bicone at PA = 188° and 233°, as well as the projected STIS velocities. These comparisons are shown in Figure 13. For the model, the STIS data along the near edge of the blueshifted cone helped to constrain the maximum velocity, and the APO data helped to constrain the opening angles, inclination, and extent of the outflow.

The final parameters of the NLR kinematic model and the adopted parameters of the galactic disk are given in

Table 3 along with the original values from (Fischer et al. 2013). Although the new PA, inclination, and HOAs differ somewhat from the original values, our view is still along the edge of the bicone. The adopted host galaxy parameters differ as well, but the overall picture of the host galaxy blocking the far, redshifted cone is the same. We have increased the maximum velocity somewhat, but the most significant change is the realization that the outflows extend to much larger distances.

4.5. Radiative Driving of the AGN

From the BPT diagnosis in section §4.3 we can infer that the high-velocity clouds seen in the *HST* STIS and APO DIS observations are primarily AGN ionized and belong to the outflow bicone (Figure 13). Considering a radiative driving mechanism (Castor et al. 1975; Abbott 1982; Proga et al. 2000) is likely responsible for pushing the gas away from the nucleus, we can compare our observed outflow kinematics to an analytical model proposed by Das et al. (2007). This model employs forces due to AGN induced radiative acceleration and gravitational deceleration from the enclosed mass in the host galaxy, to obtain the velocity profiles of the outflowing gas as a function of distance. These methods were employed by Fischer et al. (2017) and Fischer et al. (2019) for the Seyfert 2 galaxies Mrk 573 and 2MASX J0423 to determine the effects of radiative driving in the NLR/ENLR of these galaxies. García-Bernete et al. (2021) used the same approach to reproduced the ionized gas outflow as seen in MUSE- IFU observations of Seyfert galaxy NGC 5643.

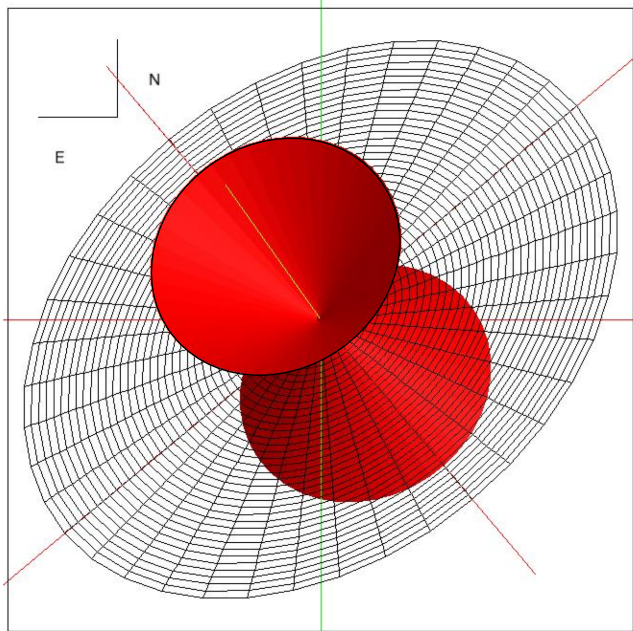
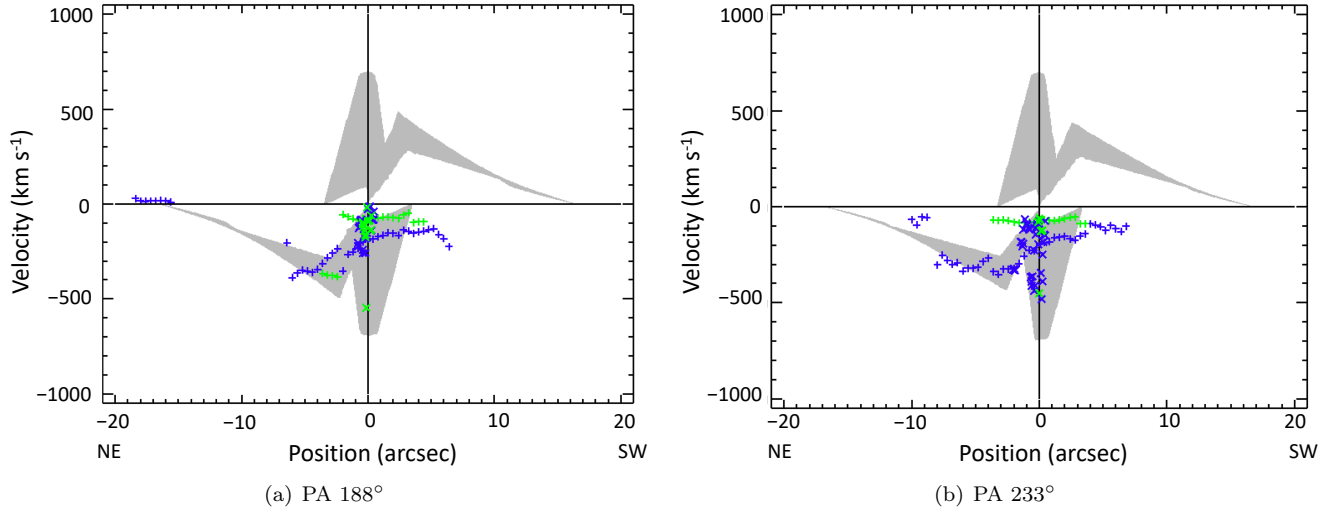
The gravitational deceleration part of this gravity-radiation relationship can be measured from the enclosed mass at a given distance r :

$$a(r) = -\frac{GM(r)}{r^2} \quad (1)$$

where we derived the enclosed mass $M(r)$ as a function of distance from the nucleus using surface brightness profiles of the host galaxy and G is the universal gravitational constant ($6.67 \times 10^{-8} \text{ cm}^3 \text{ g}^{-1} \text{ s}^{-2}$).

We obtained the parameters to fit a 2-dimensional model to the surface brightness of NGC 4051 from Bentz et al. (2009). The image decomposition was done by Bentz et al. (2009) using GALFIT (Peng et al. 2002) to fit variations of Sérsic (Sersic 1968) profiles for different brightness components of the galaxy. The radial distribution of surface brightness of a component using a Sérsic profile can be given as (Peng et al. 2010):

$$\Sigma(r) = \Sigma_e \exp \left[-\kappa \left(\left(\frac{r}{r_e} \right)^{1/n} - 1 \right) \right] \quad (2)$$



(c) Bicone model

Table 3. NGC 4051 Outflow Model Parameters

Parameters	Fischer+2013	This Work
PA (galaxy)	50°	130° (N-S in SE)
Inclination (galaxy)	5°	45° (SW closer)
PA (bicone)	80°	35°
Inclination (bicone)	78°	60° (NE closer)
HOA (max)	25°	40°
HOA (min)	10°	25°
Turnover	30 pc	380 pc
Max Height	100 pc	1090 pc
Max Velocity	550 km/s	700 km/s

NOTE—Rows are (1) major axis of galaxy from Kaneko et al. (1997), (2) inclination of galaxy from Kaneko et al. (1997), (3) major axis of bicone axis, (4) inclination of bicone axis relative to plane of sky, (5) maximum half opening angle relative to bicone axis, (6) minimum half opening angle, (7) turnover radius, (8) maximum height of bicone along its axis, and (9) maximum outflow velocity, located at turnover radius.

Figure 13. Figure (a) and (b) show the comparison of the kinematic model of biconical outflow in the NLR of NGC 4051 (gray shaded areas) with APO (“+”) and *HST* (“x”) radial velocities. Velocities are color coded to represent high (blue) and low (green) FWHM components. (a) Model extraction and velocities at APO DIS slit PA 188° plus those from STIS slit “A” projected onto this PA. (b) Model extraction and velocities at APO DIS slit PA 233° plus those from STIS slit “B” projected onto this PA. Figure (c) represents the geometry of the biconical outflow model for NGC 4051 as seen from Earth, showing the outer surface of the bicone and the disk of the host galaxy, based on the parameters in Table 3. Given the inner opening angle our view is through the wall of the near, blueshifted cone for this narrow-line Seyfert 1 galaxy and our view of the far, redshifted cone is blocked, presumably by dust in the host galactic plane.

where r_e is the effective radius for the given component, Σ_e is the surface brightness of that component at r_e , n is the Sérsic index that defines a power law and the value of constant κ is calculated such that half of the total flux lies within r_e . We retrieved the four Sérsic components and the associated parameters from [Bentz et al. \(2009\)](#). The first and second components are identified as two inner bulges or nuclear stellar clusters with $n = 1.07$ and 0.31 and $r_e = 0.03$ kpc and 0.07 kpc respectively. The third and fourth components are given as a bulge ($n = 1.80$, $r_e = 0.86$ kpc) and disk ($n = 1.00$, $r_e = 4.24$ kpc).

We calculated the mass distribution of each Sérsic component with the obtained parameters by using Equation 4-6 and A2 in [Terzić & Graham \(2005\)](#) assuming a spherical geometry. See [Fischer et al. \(2017, 2019\)](#) for more details. We calculated a mass to light ratio (M/L) of 2.86 for the bulge components and 0.63 for the disk using the $V - H$ color provided in [Bentz & Manne-Nicholas \(2018\)](#) and the relationship given in Table 1 of [Bell & de Jong \(2001\)](#), for the same V band image as in [Bentz et al. \(2009\)](#) that is adopted for this work.

Figure 14a shows the radial distributions of the enclosed mass of the four components that were identified by [Bentz et al. \(2009\)](#) and the total mass $M(r)$, which also includes the contribution from the SMBH as a point mass ($M_{\text{BH}} = 10^{6.13} M_{\odot}$) at $r < 0.01$ pc. From the mass profiles, it can be noted that the SMBH dominates the inner 1 pc and then the first and second components (nuclear stellar clusters) build up the total enclosed mass to ~ 100 pc before the mass from the outer bulge and the disk accumulates. The total enclosed mass at 1 kpc is close to the total Baryonic mass ($= 10^{9.7} M_{\odot}$) at ~ 10 kpc which accounts the total gas (based on HI cm observation) and stellar mass as reported by [Robinson et al. \(2021\)](#). We also determined the rotation curve for individual components using the corresponding mass profiles as well as for the total mass using the equation:

$$V(r) = \sqrt{G \frac{M(r)}{r}}. \quad (3)$$

Figure 14b shows the rotational circular velocities of each component separately as well as for the sum of components (including BH mass). The mass from a dark matter component is not included in these calculations, and is not expected to be a major contributor at distances < 1 kpc. The total circular velocity at 1 kpc is ~ 115 km s $^{-1}$, close to that rotational velocity H α ionized gas ~ 130 km s $^{-1}$ ([Richards et al. 2016](#), also see Figure 10), providing confidence in our enclosed mass model and mass to light ratios.

The radiative acceleration ([Arav et al. 1994](#); [Chelouche & Netzer 2001](#); [Crenshaw et al. 2003](#)) due to a central

AGN with a bolometric luminosity L on a mass at a distance r is:

$$a(r) = \frac{L\sigma_T\mathcal{M}}{4\pi r^2 c \mu m_p} \quad (4)$$

where σ_T is the Thompson scattering cross section for the electron, c is the speed of light, μ is the mean atomic weight of a proton (~ 1.4 for typical solar abundances) and m_p is the mass of the proton. \mathcal{M} is the force multiplier, which incorporates the bound-bound, bound-free and continuum opacity in addition to Thomson scattering, and depends on the ionization parameter (U) for a given spectral energy distribution. Hence the force multiplier is the ratio of total acceleration $a(r)$ to the acceleration due to Thomson scattering ([Arav et al. 1994](#); [Chelouche & Netzer 2001](#)).

Considering spherical symmetry and assuming that no other forces (hydrodynamic, thermal, drag, and magnetic) are in play, the total acceleration on a point mass at a distance r can be calculated as the sum of radiative acceleration (Equation 4) and gravitational deceleration (Equation 1). By substituting for the constants and solving for differential velocity, a model for the radial velocity of an outflowing cloud in the NLR ([Das et al. 2007](#), Equations 19-22) is given by the following expression:

$$v(r) = \sqrt{\int_{r_1}^r \left[4885 \frac{L_{44}\mathcal{M}}{r^2} - 8.6 \times 10^{-3} \frac{M(r)}{r^2} \right] dr} \quad (5)$$

where the $v(r)$ is the outflow velocity (in km s $^{-1}$) of a cloud at a distance r (in pc), L_{44} is the bolometric luminosity in 10^{44} erg s $^{-1}$, and r_1 is the launch distance of the cloud from the central SMBH. $M(r)$ is in the units of solar masses (M_{\odot}). The AGN of NGC 4051 is optically variable, which leads to a range of luminosities that have been provided by various observations in the past. Therefore, for our analysis, we determined the bolometric luminosity L_{bol} of the AGN using the [O III] luminosity $L_{[\text{O III}]}$ of the NLR and the relationship provided in [Heckman et al. \(2004\)](#) as $L_{\text{bol}} = 3500 \times L_{[\text{O III}]}$. We calculated $L_{[\text{O III}]}$ by measuring the total flux (not corrected for extinction) in the continuum-subtracted F502N [O III] image within the NLR. Using a distance of 16.6 Mpc ([Yuan et al. 2020](#)), we calculate a value of $L_{\text{bol}} = 42.9 \pm 0.3$ erg s $^{-1}$, which is in excellent agreement with the value of 42.95 erg s $^{-1}$ given in [Bentz et al. \(2013\)](#).

We used Equation 5 to numerically solve for the launch distances of the some of the observed outflowing emission-line knots as seen in our *HST* STIS and APO DIS kinematics (all of the other values in this equation are constrained). Figure 14c shows the velocity profiles of selected knots as modeled using Equation 5. We chose knots from the observed kinematics as shown in Figure 8

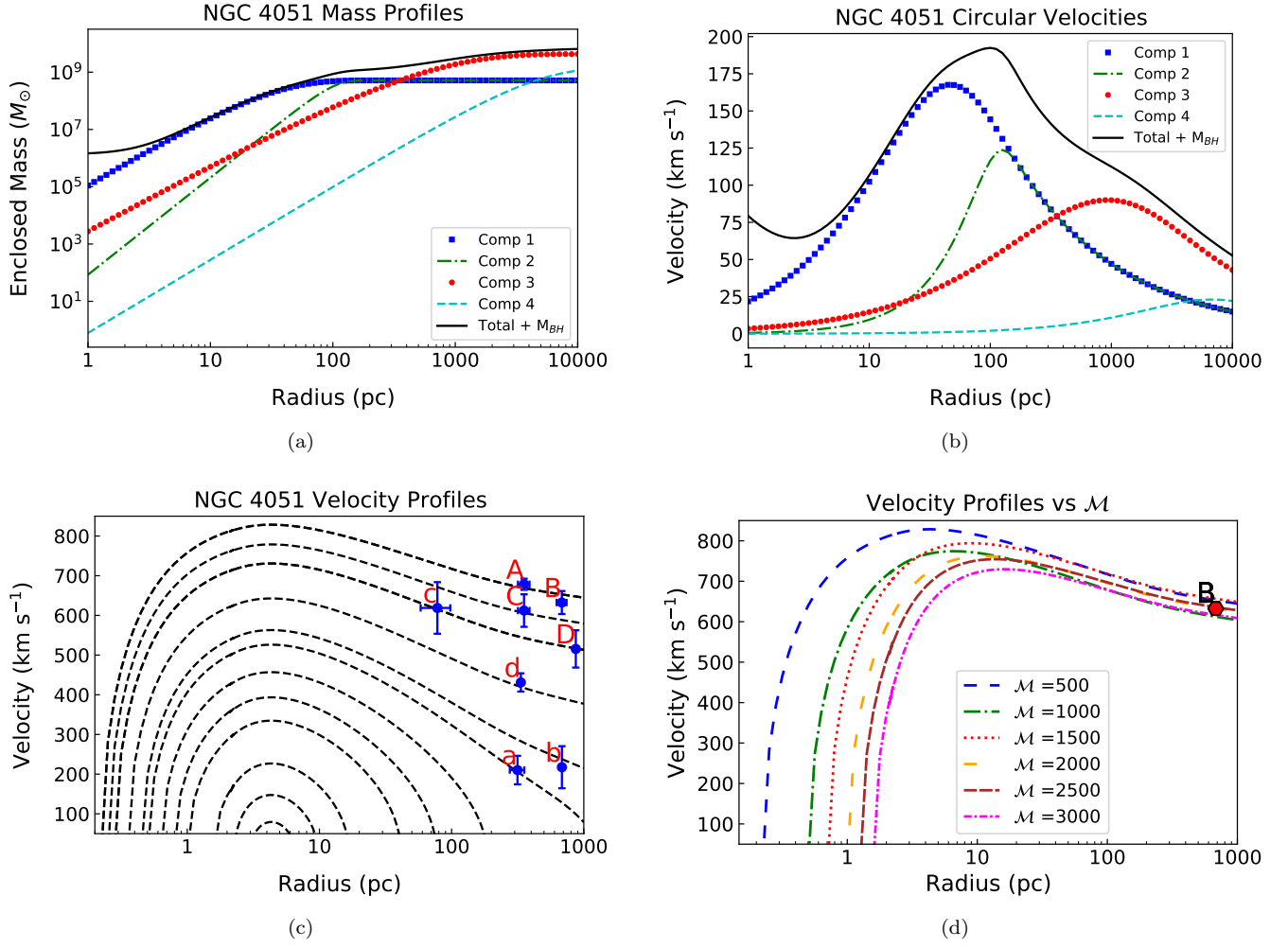


Figure 14. (a) Mass Profiles of NGC 4051, calculated using Sérsic components defined in [Bentz et al. \(2009\)](#). (b) The rotation velocities are for each mass component separately and for the total baryonic mass inside 10 kpc. (c) Velocity profiles generated with the dynamical model given in Equation 5. The capital letters are associated with the APO outflow knots and lowercase letters are assigned to the knots seen in *HST* STIS. The velocities and positions are determined using the average of selected kinematic points in Figure 8 that are assigned to each knot. The error bars are calculated from the minimum and maximum values of distance and velocity associated with the points in a given knot. The true velocities and distance are calculated using de-projection parameter from biconical model geometry given in section §4.4. (d) An example of change in launch distance of the observed outflow cloud (B) for different values of force multiplier \mathcal{M} .

for STIS parallel slits (A and B) and APO slits at PA 188° and PA 233° , which are within the blueshifted outflow cone. The positions and velocities of outflowing knots were chosen such that a distinct group of kinematic points in Figure 8 with similar FWHM and/or flux distribution are defined as a knot. The selected knots are labeled in Figure 8. The observations, the assigned name of the knot, their observed distances, and their velocities are given in Table 3.

We determined the true distances and velocities of these clouds using the parameters for the outflow bicone’s geometry; these are given in columns (5) and (6) of the table. Specifically, we determined the distance and velocity de-projection factors by assuming that the STIS

data points are from the near side of the outflow cone and the APO data are from the far side, as shown in Figure 13. We then calculated the approximate distances r_1 from which the clouds were launched/originated, using the dynamical model from Equation 5.

We adopted a conservative force multiplier $\mathcal{M} = 500$ for the model velocity profiles shown in 14c, based on the discussion in Trindade Falcao (in preparation), which considers the effects of decreasing \mathcal{M} and ionizing flux as you move deeper in the cloud, as well as the increased radiation pressure from dust in a typical [O III]-emitting NLR cloud. For comparison, these authors use a baseline value of $\mathcal{M} = 1040$, and [Fischer et al. \(2017\)](#) use a value of $\mathcal{M} = 3300$ from the ionized face of a NLR cloud.

Figure 14d shows the change in the velocity curve and launch radius r_1 with different values of \mathcal{M} . For a given position and velocity of observed cloud B', the launch distance increases with increasing \mathcal{M} almost linearly.

Figures 14c and 14d show that the relatively low-luminosity AGN in NGC 4051 is capable of driving the ionized gas in the NLR up to a distance of ~ 1 kpc with de-projected velocities up to 700 km s^{-1} . Interestingly, the emission-line clouds originate from near the nucleus at a distance of < 1 pc. It can be noted from 14c that the outflowing gas quickly achieves high velocities within ~ 10 pc of the center due to the low enclosed mass before being slowed down by the gravitational potential of the host galaxy. A higher value of \mathcal{M} may increase the launch distance up to ~ 3 pc. However, based on the condition that radiative acceleration and gravitational deceleration are responsible for the observed velocities, Figure 14c shows that no outflowing clouds can be produced beyond a distance of ~ 3 pc in this low-luminosity AGN. Hence, unlike Mrk 573 (Fischer et al. (2019)), we see no evidence of in-situ acceleration at distances of tens to hundreds of parsecs from the host galaxy disk.

5. SUMMARY AND DISCUSSION

5.1. NLR Outflow and Geometry

We identify a distinct conical structure towards the NE in a high-resolution *HST* [O III] image of NGC 4051 that resembles the $9''$ long wedge-like structure seen in [O III] ground-based observations (Christopoulou et al. 1997). The cone with an axis at PA = 35° defines the NLR in NGC 4051 and is in the same direction as the extended radio addstructure at PA $\approx 41^\circ$ (Ho & Ulvestad 2001), rather than the previously proposed E-W orientation from *HST* STIS (Fischer et al. 2013) and GEMINI observations (Barbosa et al. 2009).

From spatially-resolved kinematics of the circumnuclear gas in NGC 4051 using *HST* STIS and APO DIS long slit spectra, we identify up to two velocity components in the NLR, both of which are blueshifted with respect to the host galaxy. We find clouds with radial (line of sight) velocities up to -600 km s^{-1} in both STIS and APO observations towards the NE with respect to the central SMBH. Components with high radial velocities tend to have large widths, with FWHM up to $\sim 800 \text{ km s}^{-1}$. While the ionized gas kinematics for STIS show high flux, high velocity clouds close to the nucleus (inner $3''$), the four $2''$ wide orthogonal long slits map the [O III] ionized gas kinematics to extended distances in low flux [O III] $\lambda\lambda 4959, 5007$ and $\lambda 6563$ H α emission lines (See Figures 8 and 10). The observed kinematics are dominated by outflow and do not show a detectable rotational component in the inner $\pm 10''$ (± 800 pc). How-

ever the large scale H α kinematics closely follows the HI 21-cm rotation curve at projected distances $> 10''$ (Figure 10, Kaneko et al. 1997), indicating that the dominant kinematic component switches from outflow to rotation at the de-projected (true) distance of ~ 1 kpc.

Kinematic modeling of the combined *HST* and APO spectra shows that observed radial velocities in the inner $\pm 10''$ can be matched by conical outflow with an axis inclined by 60° with respect to the plane of the sky and with minimum and maximum opening angles of 25° and 40° , refining the earlier values by (Fischer et al. 2013). Comparison with the host galaxy geometry confirms the Fischer et al. (2013) result that the presumed redshifted cone in the SW is likely hidden by dust in the galactic plane, thus explaining our detection of only blueshifted velocities with respect to the systemic velocity of the host.

BPT diagrams and the radial distribution of [O III]/H β ratios show that AGN ionization dominates up to $\sim 10''$ from the nucleus towards the NE and NW. The moderately low [O III]/H β towards the SE and SW indicates star formation is a major contributor to the ionization at distances up to $5''$, likely because these regions are outside of the nominal bicone or in areas where the redshifted cone is mostly extinguished by the galactic disk, thereby reducing the AGN contribution. BPT diagrams show that the ionized gas beyond $10''$ is completely dominated by star formation, up to a projected distance of $\sim 100''$ (~ 8 kpc).

The NLR in NGC 4051 is well defined by AGN ionized outflows with high velocities and dispersion (intrinsic FWHM $> 250 \text{ km s}^{-1}$) up to $10''$ from the SMBH. The gas at projected distances $> 10''$ is stellar ionized, has low velocity dispersion (FWHM $< 150 \text{ km s}^{-1}$), and is rotating in the plane of the host galactic disk. We find no evidence for a significant ENLR in NGC 4051, which we define as AGN ionized gas that is rotating in the plane, and is often characterized by large FWHM (identified as “disturbed gas” by Fischer et al. 2018). An explanation is provided by our kinematic model of the outflow bicone. The axis of the bicone is pointed mostly out of the plane of the galaxy and therefore there is almost no interaction of the ionizing bicone with the rotating gas at larger distances in the host galaxy.

Given the inclination (60°), inner (25°), and outer (40°) opening angles of our biconical outflow model, our view to the NLS1 nucleus of NGC 4051 is through the wall of the blueshifted cone, which suggests that many, if not all of the unusually large number of ionized blueshifted absorption systems detected in *HST* UV spectra of NGC 4051 (Collinge et al. 2001) are due to outflowing NLR clouds in our line of sight to the nucleus as suggested by Krae-

Table 4. Parameters for the Radiative Driving Models

Observation	Knot Name	Component	Observed Distance (")	Observed Velocity (km s ⁻¹)	True Distance (pc)	True Velocity (km s ⁻¹)	Model Velocity (km s ⁻¹)	Launch Distance (pc)	Travel Time (10 ⁶ years)
HST (Slit A)	a	narrow	-0.41	-206	315	210	205	0.50	1.09
HST (Slit A)	b	wide	-0.88	-213	683	217	237	0.45	2.27
HST (Slit B)	c	wide	0.10	-606	78	618	614	0.28	0.12
HST (Slit B)	d	wide	-0.43	-422	334	431	419	0.355	0.69
APO (PA 188)	A	narrow	3.15	-376	353	678	668	0.23	0.49
APO (PA 188)	B	wide	6.09	-351	682	632	652	0.23	0.98
APO (PA 233)	C	wide	3.15	-340	353	612	606	0.25	0.54
APO (PA 233)	D	wide	7.77	-286	870	515	516	0.28	1.55

NOTE—The columns list (1) the observation (*HST* / *APO*), (2) given name for the observed knots with associated kinematics as seen in Figure 8, (3) the observed distances (in arcsec, (-) and (+) signs indicate a respective SW & NE direction for *APO* or E & W for *STIS* slits in the sky), (4) observed velocities, (5) the true/de-projected distances (in pc), (6) true/de-projected velocities using the parameters obtained for outflow bicone geometry (from kinematics model in section §4.4), (7) the velocities using the radiative driving model, (8) the calculated launch distance of these knots and (9) the total time traveled for each from launch distance to the true distance for the model velocity.

mer et al. (2012). Supporting evidence comes from the range of outflowing velocities for the UV components, 0 to -650 km s⁻¹, which is essentially the same as that of the NLR clouds.

5.2. Intermediate Line Region

We detect a spatially unresolved (FWHM $< 0.1''$, kinematic component close to the nucleus with an intermediate width (FWHM = 1010 km s⁻¹) between those of the broad and narrow emission lines in both *HST* and *APO* spectra, similar to that found by Kraemer et al. (2012) and Yang et al. (2013). We find a weak ILR component in spectral fits of [O III] $\lambda\lambda 4959, 5007$ as well as $H\beta$ lines in our observations, with a significantly small ratio for the integrated fluxes of the ILR lines of [O III]/ $H\beta \approx 0.55$. Considering a typical [O III]/ $H\beta$ ratio of ~ 10 for low density gas in the NLR, and a value of ~ 5 at the critical density ($n_e = 6.8 \times 10^5$ cm⁻³) of [O III] $\lambda 5007$ emission (Osterbrock & Ferland 2006), the observed ratio indicates an ILR gas density of $n_e \approx 10^{7.5}$ cm⁻³. Now, the size of the ILR can be calculated using the ionization parameter (U), and the number of ionizing photons per sec emitted by the AGN ($Q(H)$)³ (Osterbrock & Ferland 2006).

$$U = \frac{Q(H)}{4\pi r^2 n_H c}, \quad (6)$$

³ $Q(H) = \int_{\nu_0}^{\infty} (L_\nu / h\nu) d\nu$, where L_ν is the luminosity of the AGN as a function of frequency (the SED), h is Planck's constant, and $\nu_0 = 13.6eV/h$ is the ionization potential of hydrogen (Osterbrock & Ferland 2006, §14.3).

where r is the distance from the central AGN (cm), n_H is the hydrogen number density (cm⁻³), and c is the speed of light. We adopted a value of $\log(Q(H)) = 52.80$ photons s⁻¹ which was previously computed for NGC 4051 by Kraemer et al. (2012). Based on the absence of low ionization lines such as [S II] from the ILR, we assume an ionization parameter of $\log(U) = -2$. Using these values and estimated hydrogen density in Equation 6, we calculate the distance of the ILR from AGN to be $r_{ILR} \approx 0.24$ pc, considerably less than our upper limit based on the ILR being unresolved by *HST* *STIS*.

The inner edge of the torus is often defined by the dust sublimation radius (r_{sub}) which has previously been calculated as ~ 0.01 pc based on the UV luminosity of NGC 4051 (Krongold et al. 2007). Reverberation mapping of the V and K band variability provides a similar value of 0.011 ± 0.004 pc (Suganuma et al. 2006). An “effective” inner radius of 0.032 ± 0.003 pc has been determined by fitting ring model to K-band interferometry (Kishimoto et al. 2009). However, it is not clear how far the torus extends and how it may connect to the fueling flow from the galaxy. Thus, it is likely that the ILR originates from the outer portion of the dusty torus (García-Bernete et al. 2019) or from the molecular flow that is fueling the torus. Although the ILR is unresolved, it has a net blueshifted velocity of ~ -110 km/sec, indicating that it may have an outflow component as well.

(Riffel et al. 2008) find a blueshifted (up to -100 km s⁻¹), slightly curved structure in their Gemini NIFS observations of warm H₂ emission extending up to $2''$ along

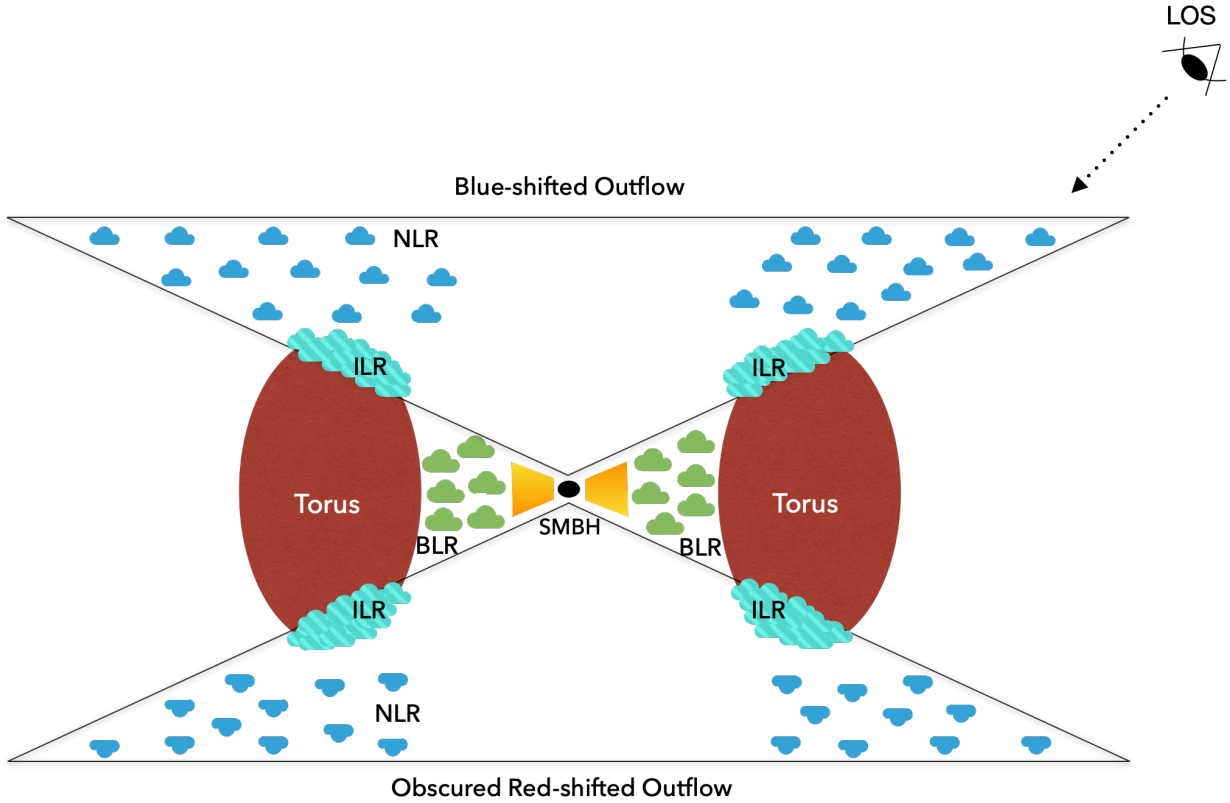


Figure 15. A cross-section interpretation of the nuclear regions in NGC 4051 which include the SMBH (black dot) with the accretion disk (yellow), BLR (green clouds), torus (brown), ILR (cyan clouds) and NLR outflows (blue clouds). The various regions in this cartoon are not on a linear scale. A $H\beta$ reverberation mapped BLR radius has been given by Denney et al. (2009) as $R_{BLR} = 1.87^{+0.54}_{-0.50}$ light days and the inner edge of the torus is approximately located at 0.01-0.03 pc (Suganuma et al. 2006; Krongold et al. 2007; Kishimoto et al. 2009) from SMBH. As discussed in section §5.2, we measured the ILR distance at $r_{ILR} \approx 0.5$ pc, which is either located close to the outer edge of the torus or is part of its fueling material. The NLR expands from close to the ILR up to 1 kpc, pointing out of the host galaxy disk.

the eastern edge of the ionized bicone. They present arguments for and against inflow and outflow of the H_2 gas, and slightly prefer the inflow interpretation. We suggest that outflow is more likely, because the H_2 emission is nearly coincident with the ionized gas, suggesting a common origin as found in our NIFS studies of Mrk 573 (Fischer et al. 2017) and Mrk 3 (Gnilka et al. 2020).

5.3. Outflow Origins

As seen in Figure 14c, the clouds launched within ~ 0.5 pc of the nucleus (for $\mathcal{M} = 500$) can travel up to ~ 1 kpc in NGC 4051. However, as we increase the launch distance, the clouds start to turn over and reach the systemic velocity of the galaxy within 100 pc. This is different than the case of Mrk 573, which has a much higher luminosity ($\log(L_{bol}) = 45.5 \pm 0.6$ erg s^{-1}), where the gas clouds can be launched from within 600 pc (see Figure 15

in Fischer et al. 2017). Interestingly, though, nearly all of the bright clouds have traveled for distances < 100 in Mrk 573, compared to hundreds of pc in NGC 4051. The maximum launch radius increases in Seyfert 2 galaxy 2MASX J0423 ($L_{bol} = 10^{45.55}$ erg s^{-1}) by almost 10 times, due to the lower gravitational potential of the host disk (Fischer et al. 2019). Recently, (García-Bernete et al. 2021) showed that the ionized gas outflows as seen in MUSE/IFU observations of NGC 5643 ($L_{bol} = 8.14 \times 10^{43}$ erg s^{-1}) were launched within 4 pc of the nucleus.

This trend is shown in Figure 16, which illustrates that for a comparable mass distribution there is a luminosity dependence of the maximum distance to which the AGN is capable of driving the gas away in the form of ionized outflows, as expected from our radiative driving model. Even though intermediate and low luminosity AGN can

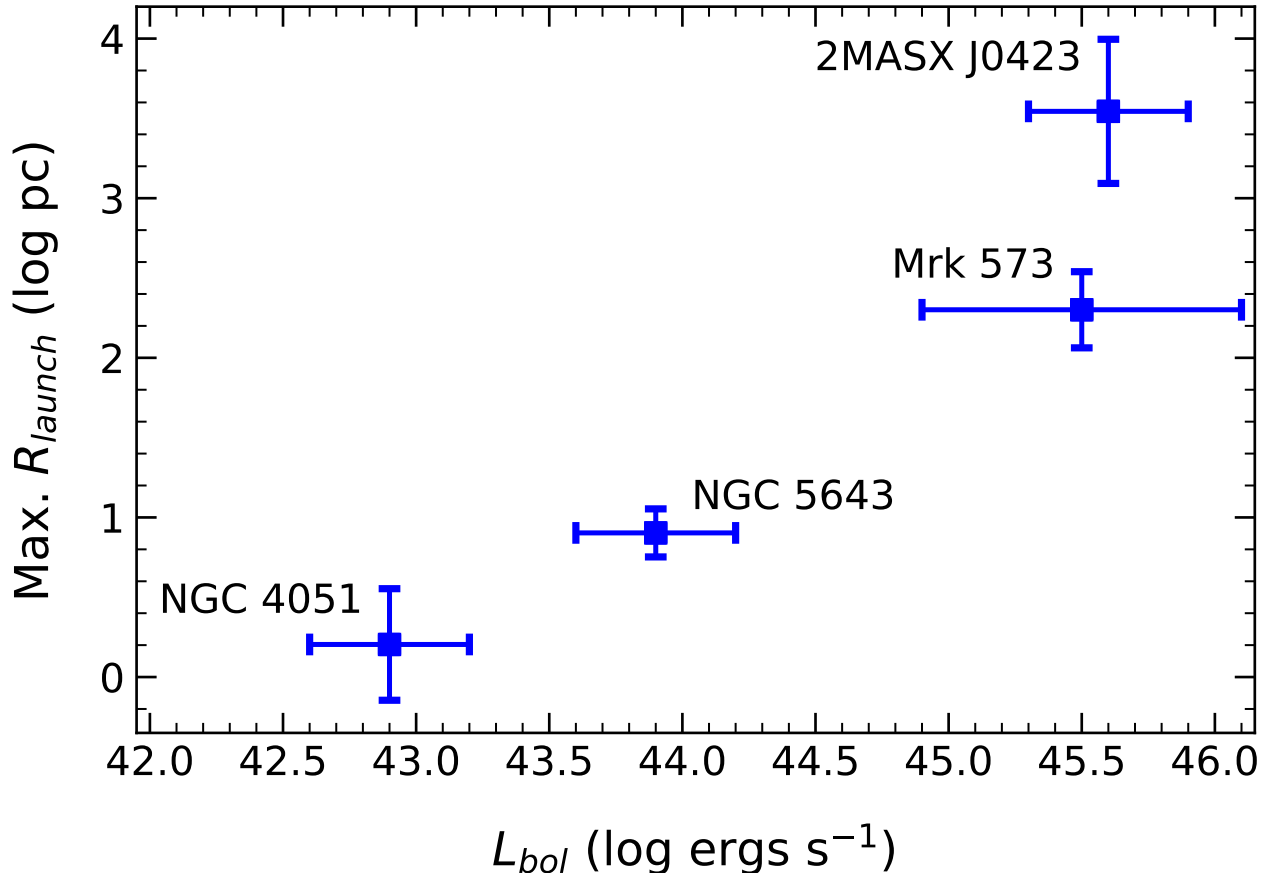


Figure 16. A comparison of the maximum launch radius, R_{launch} from which the outflow clouds can be radiatively driven in the four AGN of different bolometric luminosities (L_{bol}). The launch distances for NGC 4051 are calculated from this work and rest were extracted from [García-Bernete et al. \(2021\)](#) (NGC 5643), [Fischer et al. \(2017\)](#) (Mrk 573) and [Fischer et al. \(2019\)](#) (2MASX J0423). The uncertainties in the launch distances were determined based on \mathcal{M} variation. For NGC 4051, Mrk 573 and 2MASX J0423, lower limit corresponds to $\mathcal{M} = 500$ and an upper limit corresponds to $\mathcal{M} = 3300$. For NGC 5643, \mathcal{M} was given in the range of 200 to 400 (See Figure 12, [García-Bernete et al. 2021](#)). The uncertainties in bolometric luminosities was adopted as ± 0.3 dex for NGC 4051 and 2MASX J0423 from uncertainties in the [O III] to bolometric luminosity relationship and correction factor. The bolometric luminosity for NGC 5643 is the same as chosen by [García-Bernete et al. \(2021\)](#) analysis, which lead to uncertainties = ± 0.3 dex from scattering in $L_{14-195 \text{ keV}}$ ([Ricci et al. 2017](#)). The uncertainties for L_{bol} for Mrk 573 is given as ± 0.6 dex in [Kraemer et al. \(2009\)](#).

apparently drive the gas up to hundreds of parsecs, these clouds are originating from within a few pc of the nucleus and presumably not disrupting the gas reservoir outside those radii. On the other hand a brighter AGN is more successful in radiatively driving the gas from within hundreds of pc and thus disrupting the molecular reservoirs and impacting nuclear star formation on a large scale. Nonetheless, the total outflow travel distances tend to be much smaller than the full extents of AGN ionization and typical bulge sizes in these galaxies. That said, AGN driven outflows may potentially produce negative feedback by evacuating some fraction of the gas in bulges and affect nuclear star formation in galaxies with brighter AGN. However, this hypothesis requires further analysis of AGN on the higher end of luminosity range, as well as

determinations of spatially-resolved mass outflow and kinetic energy rates over a broad range in AGN luminosity ([Revalski et al. 2021](#)).

Figure 15 shows a geometric representation of the BLR, torus, ILR, and NLR locations in the nuclear regions of NGC 4051. It is possible that the ILR is not physically separated from the NLR but defines the very inner boundaries of the NLR outflows. Comparing the launch distances as given in Table 4 with the ILR radius (~ 0.24 pc) as discussed in section §5.2, it is likely that the outflowing clouds originated close to the ILR. Thus in NGC 4051, both ILR and NLR were potentially formed as a result of AGN radiation interaction with the molecular reservoirs in the vicinity of the torus. In

this scenario, the ILR represents the location of recently launched clouds.

6. CONCLUSIONS

We present a detailed analysis of ionized gas outflow properties in the low luminosity NLS1 galaxy NGC 4051 and compare the effectiveness of radiative driving of the gas in the gravitational potential of the host galaxy with previous studies of higher luminosity AGN. Our main conclusions are:

1. The spatially resolved kinematics of ionized gas in the NLR of NGC 4051 show two blueshifted velocity components but no redshifted emissions. We find AGN ionization and outflow extends up to a projected distance of $\sim 10''$ (~ 800 pc) towards the NE. The outflow structure follows the [O III] cone seen in a high resolution *HST* WFC3 image and the alignment of the extended radio structure.
2. We developed a biconical outflow model to determine the true velocities and distances of the observed outflowing clouds. The maximum extent of the observed outflows is ~ 1 kpc, which is much larger than the ~ 100 pc from (Fischer et al. 2013) due to the addition of the APO data. The peak velocities are ~ 680 km s $^{-1}$ at a distance of ~ 350 pc from the nucleus.
3. A radiation pressure driven wind plus gravitational deceleration model for the AGN ionized gas shows that the observed outflowing clouds in NGC 4051 originate within ~ 0.5 pc (for a force multiplier $\mathcal{M} = 500$, up to 3 pc for $\mathcal{M} = 3000$) from the SMBH and can travel up to ~ 1 kpc. However the radiative driving fails beyond ~ 3 pc radius from the center and no outflowing clouds can be produced at larger distances. Hence, unlike higher luminosity AGN, there is no evidence of in situ ionization and acceleration of gas from large distances in the host disk.
4. A comparison of maximum launch distance for this low luminosity AGN with those that were previously measured for higher luminosity AGN shows a strong positive correlation with luminosity. This means, for a comparable mass distribution, a higher luminosity AGN is more efficient in ionizing the gas and producing the outflows at larger distances from the nucleus. This implies that the AGN feedback is more efficient for brighter AGN. However a larger sample over a wider luminosity range is required to quantify any correlation.
5. We find a moderate-density intermediate line region (ILR) component in the H β and [O III] emission lines, with density $n_{\text{H}} \approx 10^{7.5}$ cm $^{-3}$ and radius of ~ 0.24 pc. The ILR component has FWHM = 1010 km s $^{-1}$ and is blueshifted by -110 km s $^{-1}$ with respect to the systemic velocity of the host galaxy. This component is unresolved in both *HST* STIS and APO DIS spectra, with a brightness profile that follows the instrument/seeing PSF. The similar locations of the ILR and the outflow launch distances of the NLR outflows suggest they have a common origin, which is the gas evacuation caused by AGN radiation acting on the torus or its fueling flow.
6. Our line of sight passes through the wall of our biconical outflow model, which suggests that most, if not all, of the unusually large number of ionized UV absorbers seen in *HST* spectra of NGC 4051 are due to NLR clouds seen in absorption. The nearly identical range in outflow velocity (0 to -650 km s $^{-1}$) of the NLR clouds and UV absorbers supports this interpretation.
7. Beyond ~ 1 kpc, the gas is stellar ionized, rotating in the galactic plane, and has low FWHM. There is no significant evidence for AGN ionized gas rotating in the plane, and therefore no evidence for a significant ENLR in NGC 4051. This can be explained by our kinematic model of biconical outflow, as the near, blueshifted cone points up out of the galactic plane and therefore does not create a region of extended, AGN ionized gas in the plane.

ACKNOWLEDGMENTS

The authors would like to thank the anonymous referee for their constructive feedback on this paper. B.M. is also grateful of Dr. Misty Bentz and Justin H. Robinson for their helpful advice and discussions. This research has made use of NASA's Astrophysics Data System. This research has made use of the NASA/IPAC Extragalactic Database (NED), which is operated by the Jet Propulsion Laboratory, California Institute of Technology, under contract with the National Aeronautics and Space Administration. IRAF is distributed by the National Optical Astronomy Observatories, which are operated by the Association of Universities for Research in Astronomy, Inc., under cooperative agreement with the National Science Foundation

Facilities: APO(DIS, ARCTIC), *HST* (STIS, WFC3)

Software: IRAF (Tody 1986, 1993), MultiNest (Feroz et al. 2019), SAOImage DS9 (Smithsonian Astrophysical Observatory 2000), Mathematica (Wolfram Research

2014), Python (Van Rossum & Drake 2009, <https://www.python.org>), Astropy (Astropy Collaboration et al. 2013), Interactive Data Language (IDL, <https://www.harrisgeospatial.com/Software-Technology/IDL>).

REFERENCES

- Abbott, D. C. 1982, ApJ, 259, 282, doi: [10.1086/160166](https://doi.org/10.1086/160166)
- Adhikari, T. P., Rózańska, A., Czerny, B., Hryniewicz, K., & Ferland, G. J. 2016, ApJ, 831, 68, doi: [10.3847/0004-637X/831/1/68](https://doi.org/10.3847/0004-637X/831/1/68)
- Anderson, J. P., Haberman, S. M., James, P. A., & Hamuy, M. 2012, MNRAS, 424, 1372, doi: [10.1111/j.1365-2966.2012.21324.x](https://doi.org/10.1111/j.1365-2966.2012.21324.x)
- Antonucci, R. R. J., & Miller, J. S. 1985, ApJ, 297, 621, doi: [10.1086/163559](https://doi.org/10.1086/163559)
- Arav, N., Li, Z.-Y., & Begelman, M. C. 1994, ApJ, 432, 62, doi: [10.1086/174549](https://doi.org/10.1086/174549)
- Arribas, S., Mediavilla, E., & Garcia-Lorenzo, B. 1996, ApJ, 463, 509, doi: [10.1086/177265](https://doi.org/10.1086/177265)
- Astropy Collaboration, Robitaille, T. P., Tollerud, E. J., et al. 2013, A&A, 558, A33, doi: [10.1051/0004-6361/201322068](https://doi.org/10.1051/0004-6361/201322068)
- Baldwin, J. A., Phillips, M. M., & Terlevich, R. 1981, PASP, 93, 5, doi: [10.1086/130766](https://doi.org/10.1086/130766)
- Barbosa, F. K. B., Storchi-Bergmann, T., Cid Fernandes, R., Winge, C., & Schmitt, H. 2009, MNRAS, 396, 2, doi: [10.1111/j.1365-2966.2009.14485.x](https://doi.org/10.1111/j.1365-2966.2009.14485.x)
- Barth, A. J., Bennert, V. N., Canalizo, G., et al. 2015, ApJS, 217, 26, doi: [10.1088/0067-0049/217/2/26](https://doi.org/10.1088/0067-0049/217/2/26)
- Bartunov, O. S., Tsvetkov, D. Y., & Filimonova, I. V. 1994, PASP, 106, 1276, doi: [10.1086/133505](https://doi.org/10.1086/133505)
- Bell, E. F., & de Jong, R. S. 2001, ApJ, 550, 212, doi: [10.1086/319728](https://doi.org/10.1086/319728)
- Bennert, N., Falcke, H., Schulz, H., Wilson, A. S., & Wills, B. J. 2002, ApJL, 574, L105, doi: [10.1086/342420](https://doi.org/10.1086/342420)
- Bentz, M. C., & Manne-Nicholas, E. 2018, ApJ, 864, 146, doi: [10.3847/1538-4357/aad808](https://doi.org/10.3847/1538-4357/aad808)
- Bentz, M. C., Peterson, B. M., Netzer, H., Pogge, R. W., & Vestergaard, M. 2009, ApJ, 697, 160, doi: [10.1088/0004-637X/697/1/160](https://doi.org/10.1088/0004-637X/697/1/160)
- Bentz, M. C., Denney, K. D., Grier, C. J., et al. 2013, ApJ, 767, 149, doi: [10.1088/0004-637X/767/2/149](https://doi.org/10.1088/0004-637X/767/2/149)
- Blandford, R., Meier, D., & Readhead, A. 2019, ARA&A, 57, 467, doi: [10.1146/annurev-astro-081817-051948](https://doi.org/10.1146/annurev-astro-081817-051948)
- Breedt, E., McHardy, I. M., Arévalo, P., et al. 2010, MNRAS, 403, 605, doi: [10.1111/j.1365-2966.2009.16146.x](https://doi.org/10.1111/j.1365-2966.2009.16146.x)
- Buchner, J., Georgakakis, A., Nandra, K., et al. 2014, A&A, 564, A125, doi: [10.1051/0004-6361/201322971](https://doi.org/10.1051/0004-6361/201322971)
- Castor, J. I., Abbott, D. C., & Klein, R. I. 1975, ApJ, 195, 157, doi: [10.1086/153315](https://doi.org/10.1086/153315)
- Chelouche, D., & Netzer, H. 2001, MNRAS, 326, 916, doi: [10.1046/j.1365-8711.2001.04586.x](https://doi.org/10.1046/j.1365-8711.2001.04586.x)
- Christopoulou, P. E., Holloway, A. J., Steffen, W., et al. 1997, MNRAS, 284, 385, doi: [10.1093/mnras/284.2.385](https://doi.org/10.1093/mnras/284.2.385)
- Colbert, E. J. M., Baum, S. A., Gallimore, J. F., et al. 1996, ApJS, 105, 75, doi: [10.1086/192307](https://doi.org/10.1086/192307)
- Collinge, M. J., Brandt, W. N., Kaspi, S., et al. 2001, ApJ, 557, 2, doi: [10.1086/321635](https://doi.org/10.1086/321635)
- Costantini, E. 2010, SSRv, 157, 265, doi: [10.1007/s11214-010-9706-3](https://doi.org/10.1007/s11214-010-9706-3)
- Crenshaw, D. M., Fischer, T. C., Kraemer, S. B., & Schmitt, H. R. 2015, ApJ, 799, 83, doi: [10.1088/0004-637X/799/1/83](https://doi.org/10.1088/0004-637X/799/1/83)
- Crenshaw, D. M., & Kraemer, S. B. 2000, ApJL, 532, L101, doi: [10.1086/312581](https://doi.org/10.1086/312581)
- . 2005, ApJ, 625, 680, doi: [10.1086/429581](https://doi.org/10.1086/429581)
- . 2007, ApJ, 659, 250, doi: [10.1086/511970](https://doi.org/10.1086/511970)
- . 2012, ApJ, 753, 75, doi: [10.1088/0004-637X/753/1/75](https://doi.org/10.1088/0004-637X/753/1/75)
- Crenshaw, D. M., Kraemer, S. B., & George, I. M. 2003, ARA&A, 41, 117, doi: [10.1146/annurev.astro.41.082801.100328](https://doi.org/10.1146/annurev.astro.41.082801.100328)
- Crenshaw, D. M., Kraemer, S. B., Schmitt, H. R., et al. 2009, ApJ, 698, 281, doi: [10.1088/0004-637X/698/1/281](https://doi.org/10.1088/0004-637X/698/1/281)
- Crenshaw, D. M., & Peterson, B. M. 1986, PASP, 98, 185, doi: [10.1086/131742](https://doi.org/10.1086/131742)
- Crenshaw, D. M., Kraemer, S. B., Hutchings, J. B., et al. 2000, AJ, 120, 1731, doi: [10.1086/301574](https://doi.org/10.1086/301574)
- Das, V., Crenshaw, D. M., & Kraemer, S. B. 2007, ApJ, 656, 699, doi: [10.1086/510580](https://doi.org/10.1086/510580)
- Das, V., Crenshaw, D. M., Hutchings, J. B., et al. 2005, AJ, 130, 945, doi: [10.1086/432255](https://doi.org/10.1086/432255)
- de Vaucouleurs, G., de Vaucouleurs, A., Corwin, Herold G., J., et al. 1991, Third Reference Catalogue of Bright Galaxies
- Denney, K. D., Watson, L. C., Peterson, B. M., et al. 2009, ApJ, 702, 1353, doi: [10.1088/0004-637X/702/2/1353](https://doi.org/10.1088/0004-637X/702/2/1353)
- Dressel, L. 2012, Wide Field Camera 3 Instrument Handbook for Cycle 21 v. 5.0 (Space Telescope Science Institute)
- Fabian, A. C. 2012, ARA&A, 50, 455, doi: [10.1146/annurev-astro-081811-125521](https://doi.org/10.1146/annurev-astro-081811-125521)

- Ferland, G. J., Korista, K. T., Verner, D. A., et al. 1998, *PASP*, 110, 761, doi: [10.1086/316190](https://doi.org/10.1086/316190)
- Feroz, F., & Hobson, M. P. 2008, *MNRAS*, 384, 449, doi: [10.1111/j.1365-2966.2007.12353.x](https://doi.org/10.1111/j.1365-2966.2007.12353.x)
- Feroz, F., Hobson, M. P., & Bridges, M. 2009, *MNRAS*, 398, 1601, doi: [10.1111/j.1365-2966.2009.14548.x](https://doi.org/10.1111/j.1365-2966.2009.14548.x)
- Feroz, F., Hobson, M. P., Cameron, E., & Pettitt, A. N. 2019, *The Open Journal of Astrophysics*, 2, 10, doi: [10.21105/astro.1306.2144](https://doi.org/10.21105/astro.1306.2144)
- Ferrarese, L., & Merritt, D. 2000, *ApJL*, 539, L9, doi: [10.1086/312838](https://doi.org/10.1086/312838)
- Fischer, T., Smith, K. L., Kraemer, S., et al. 2019, *ApJ*, 887, 200, doi: [10.3847/1538-4357/ab55e3](https://doi.org/10.3847/1538-4357/ab55e3)
- Fischer, T. C., Crenshaw, D. M., Kraemer, S. B., & Schmitt, H. R. 2013, *ApJS*, 209, 1, doi: [10.1088/0067-0049/209/1/1](https://doi.org/10.1088/0067-0049/209/1/1)
- Fischer, T. C., Crenshaw, D. M., Kraemer, S. B., et al. 2011, *ApJ*, 727, 71, doi: [10.1088/0004-637X/727/2/71](https://doi.org/10.1088/0004-637X/727/2/71)
- Fischer, T. C., Machuca, C., Diniz, M. R., et al. 2017, *ApJ*, 834, 30, doi: [10.3847/1538-4357/834/1/30](https://doi.org/10.3847/1538-4357/834/1/30)
- Fischer, T. C., Kraemer, S. B., Schmitt, H. R., et al. 2018, *ApJ*, 856, 102, doi: [10.3847/1538-4357/aab03e](https://doi.org/10.3847/1538-4357/aab03e)
- Ganguly, R., & Brotherton, M. S. 2008, *ApJ*, 672, 102, doi: [10.1086/524106](https://doi.org/10.1086/524106)
- García-Bernete, I., Ramos Almeida, C., Alonso-Herrero, A., et al. 2019, *MNRAS*, 486, 4917, doi: [10.1093/mnras/stz1003](https://doi.org/10.1093/mnras/stz1003)
- García-Bernete, I., Alonso-Herrero, A., García-Burillo, S., et al. 2021, *A&A*, 645, A21, doi: [10.1051/0004-6361/202038256](https://doi.org/10.1051/0004-6361/202038256)
- Gebhardt, K., Bender, R., Bower, G., et al. 2000, *ApJL*, 539, L13, doi: [10.1086/312840](https://doi.org/10.1086/312840)
- Gnilka, C. L., Crenshaw, D. M., Fischer, T. C., et al. 2020, *ApJ*, 893, 80, doi: [10.3847/1538-4357/ab8000](https://doi.org/10.3847/1538-4357/ab8000)
- Haniff, C. A., Wilson, A. S., & Ward, M. J. 1988, *ApJ*, 334, 104, doi: [10.1086/166821](https://doi.org/10.1086/166821)
- Heckman, T. M., Kauffmann, G., Brinchmann, J., et al. 2004, *ApJ*, 613, 109, doi: [10.1086/422872](https://doi.org/10.1086/422872)
- Heckman, T. M., Miley, G. K., van Breugel, W. J. M., & Butcher, H. R. 1981, *ApJ*, 247, 403, doi: [10.1086/159050](https://doi.org/10.1086/159050)
- Herrera-Camus, R., Tacconi, L., Genzel, R., et al. 2019, *ApJ*, 871, 37, doi: [10.3847/1538-4357/aaf6a7](https://doi.org/10.3847/1538-4357/aaf6a7)
- Ho, L. C., & Ulvestad, J. S. 2001, *ApJS*, 133, 77, doi: [10.1086/319185](https://doi.org/10.1086/319185)
- Hutchings, J. B., Crenshaw, D. M., Kaiser, M. E., et al. 1998, *ApJL*, 492, L115, doi: [10.1086/311100](https://doi.org/10.1086/311100)
- Kaneko, N., Aoki, K., Kosugi, G., et al. 1997, *AJ*, 114, 94, doi: [10.1086/118455](https://doi.org/10.1086/118455)
- Kang, D., & Woo, J.-H. 2018, *ApJ*, 864, 124, doi: [10.3847/1538-4357/aad561](https://doi.org/10.3847/1538-4357/aad561)
- Karouzos, M., Woo, J.-H., & Bae, H.-J. 2016, *ApJ*, 819, 148, doi: [10.3847/0004-637X/819/2/148](https://doi.org/10.3847/0004-637X/819/2/148)
- Kauffmann, G., Heckman, T. M., Tremonti, C., et al. 2003, *MNRAS*, 346, 1055, doi: [10.1111/j.1365-2966.2003.07154.x](https://doi.org/10.1111/j.1365-2966.2003.07154.x)
- Kewley, L. J., Dopita, M. A., Sutherland, R. S., Heisler, C. A., & Trevena, J. 2001, *ApJ*, 556, 121, doi: [10.1086/321545](https://doi.org/10.1086/321545)
- Kewley, L. J., Groves, B., Kauffmann, G., & Heckman, T. 2006, *MNRAS*, 372, 961, doi: [10.1111/j.1365-2966.2006.10859.x](https://doi.org/10.1111/j.1365-2966.2006.10859.x)
- King, A., & Pounds, K. 2015, *ARA&A*, 53, 115, doi: [10.1146/annurev-astro-082214-122316](https://doi.org/10.1146/annurev-astro-082214-122316)
- Kishimoto, M., Hönig, S. F., Antonucci, R., et al. 2009, *A&A*, 507, L57, doi: [10.1051/0004-6361/200913512](https://doi.org/10.1051/0004-6361/200913512)
- Kohno, K., Nakanishi, K., & Imanishi, M. 2007, in *Astronomical Society of the Pacific Conference Series*, Vol. 373, *The Central Engine of Active Galactic Nuclei*, ed. L. C. Ho & J. W. Wang, 647. <https://arxiv.org/abs/0704.2818>
- Kormendy, J., & Ho, L. C. 2013, *ARA&A*, 51, 511, doi: [10.1146/annurev-astro-082708-101811](https://doi.org/10.1146/annurev-astro-082708-101811)
- Kormendy, J., & Richstone, D. 1995, *ARA&A*, 33, 581, doi: [10.1146/annurev.aa.33.090195.003053](https://doi.org/10.1146/annurev.aa.33.090195.003053)
- Kraemer, S. B., Schmitt, H. R., & Crenshaw, D. M. 2008, *ApJ*, 679, 1128, doi: [10.1086/587802](https://doi.org/10.1086/587802)
- Kraemer, S. B., Trippe, M. L., Crenshaw, D. M., et al. 2009, *ApJ*, 698, 106, doi: [10.1088/0004-637X/698/1/106](https://doi.org/10.1088/0004-637X/698/1/106)
- Kraemer, S. B., Crenshaw, D. M., Dunn, J. P., et al. 2012, *ApJ*, 751, 84, doi: [10.1088/0004-637X/751/2/84](https://doi.org/10.1088/0004-637X/751/2/84)
- Krongold, Y., Nicastro, F., Elvis, M., et al. 2007, *ApJ*, 659, 1022, doi: [10.1086/512476](https://doi.org/10.1086/512476)
- Kuzio de Naray, R., Arsenault, C. A., Spekkens, K., et al. 2012, *DiskFit: Modeling Asymmetries in Disk Galaxies*. <http://ascl.net/1209.011>
- Laha, S., Guainazzi, M., Chakravorty, S., Dewangan, G. C., & Kembhavi, A. K. 2016, *MNRAS*, 457, 3896, doi: [10.1093/mnras/stw211](https://doi.org/10.1093/mnras/stw211)
- Laha, S., Guainazzi, M., Dewangan, G. C., Chakravorty, S., & Kembhavi, A. K. 2014, *MNRAS*, 441, 2613, doi: [10.1093/mnras/stu669](https://doi.org/10.1093/mnras/stu669)
- Laha, S., Reynolds, C. S., Reeves, J., et al. 2021, *Nature Astronomy*, 5, 13, doi: [10.1038/s41550-020-01255-2](https://doi.org/10.1038/s41550-020-01255-2)
- Leighly, K. M. 1999, *ApJS*, 125, 317, doi: [10.1086/313287](https://doi.org/10.1086/313287)
- Magorrian, J., Tremaine, S., Richstone, D., et al. 1998, *AJ*, 115, 2285, doi: [10.1086/300353](https://doi.org/10.1086/300353)
- Marconi, A., & Hunt, L. K. 2003, *ApJL*, 589, L21, doi: [10.1086/375804](https://doi.org/10.1086/375804)
- Marziani, P., Sulentic, J. W., Stirpe, G. M., Zamfir, S., & Calvani, M. 2009, *A&A*, 495, 83, doi: [10.1051/0004-6361:200810764](https://doi.org/10.1051/0004-6361:200810764)

- May, D., Steiner, J. E., Menezes, R. B., Williams, D. R. A., & Wang, J. 2020, *MNRAS*, 496, 1488, doi: [10.1093/mnras/staa1545](https://doi.org/10.1093/mnras/staa1545)
- Meléndez, M., Kraemer, S. B., Schmitt, H. R., et al. 2008a, *ApJ*, 689, 95, doi: [10.1086/592724](https://doi.org/10.1086/592724)
- Meléndez, M., Kraemer, S. B., Armentrout, B. K., et al. 2008b, *ApJ*, 682, 94, doi: [10.1086/588807](https://doi.org/10.1086/588807)
- Mullaney, J. R., Alexander, D. M., Fine, S., et al. 2013, *MNRAS*, 433, 622, doi: [10.1093/mnras/stt751](https://doi.org/10.1093/mnras/stt751)
- Mullaney, J. R., & Ward, M. J. 2008, *MNRAS*, 385, 53, doi: [10.1111/j.1365-2966.2007.12777.x](https://doi.org/10.1111/j.1365-2966.2007.12777.x)
- Müller-Sánchez, F., Prieto, M. A., Hicks, E. K. S., et al. 2011, *ApJ*, 739, 69, doi: [10.1088/0004-637X/739/2/69](https://doi.org/10.1088/0004-637X/739/2/69)
- Nelson, C. H., Weistrop, D., Hutchings, J. B., et al. 2000, *ApJ*, 531, 257, doi: [10.1086/308456](https://doi.org/10.1086/308456)
- Oke, J. B. 1990, *AJ*, 99, 1621, doi: [10.1086/115444](https://doi.org/10.1086/115444)
- Osterbrock, D. E., & Ferland, G. J. 2006, *Astrophysics of gaseous nebulae and active galactic nuclei* (University Science Books)
- Osterbrock, D. E., & Pogge, R. W. 1985, *ApJ*, 297, 166, doi: [10.1086/163513](https://doi.org/10.1086/163513)
- Park, D., Woo, J.-H., Treu, T., et al. 2012, *ApJ*, 747, 30, doi: [10.1088/0004-637X/747/1/30](https://doi.org/10.1088/0004-637X/747/1/30)
- Peng, C. Y., Ho, L. C., Impey, C. D., & Rix, H.-W. 2002, *AJ*, 124, 266, doi: [10.1086/340952](https://doi.org/10.1086/340952)
- . 2010, *AJ*, 139, 2097, doi: [10.1088/0004-6256/139/6/2097](https://doi.org/10.1088/0004-6256/139/6/2097)
- Peters, W., & Kuzio de Naray, R. 2017, *MNRAS*, 469, 3541, doi: [10.1093/mnras/stx821](https://doi.org/10.1093/mnras/stx821)
- Peterson, B. M., McHardy, I. M., Wilkes, B. J., et al. 2000, *ApJ*, 542, 161, doi: [10.1086/309518](https://doi.org/10.1086/309518)
- Peterson, B. M., Ferrarese, L., Gilbert, K. M., et al. 2004, *ApJ*, 613, 682, doi: [10.1086/423269](https://doi.org/10.1086/423269)
- Pogge, R. W. 1988, *ApJ*, 328, 519, doi: [10.1086/166309](https://doi.org/10.1086/166309)
- . 1989, *ApJ*, 345, 730, doi: [10.1086/167945](https://doi.org/10.1086/167945)
- Pounds, K. A., & King, A. R. 2013, *MNRAS*, 433, 1369, doi: [10.1093/mnras/stt807](https://doi.org/10.1093/mnras/stt807)
- Pounds, K. A., & Vaughan, S. 2011, *MNRAS*, 413, 1251, doi: [10.1111/j.1365-2966.2011.18211.x](https://doi.org/10.1111/j.1365-2966.2011.18211.x)
- Proga, D., Stone, J. M., & Kallman, T. R. 2000, *ApJ*, 543, 686, doi: [10.1086/317154](https://doi.org/10.1086/317154)
- Revalski, M., Crenshaw, D. M., Kraemer, S. B., et al. 2018a, *ApJ*, 856, 46, doi: [10.3847/1538-4357/aab107](https://doi.org/10.3847/1538-4357/aab107)
- Revalski, M., Dashtamirova, D., Crenshaw, D. M., et al. 2018b, *ApJ*, 867, 88, doi: [10.3847/1538-4357/aae3e6](https://doi.org/10.3847/1538-4357/aae3e6)
- Revalski, M., Meena, B., Martinez, F., et al. 2021, *ApJ*, 910, 139, doi: [10.3847/1538-4357/abdcad](https://doi.org/10.3847/1538-4357/abdcad)
- Ricci, C., Trakhtenbrot, B., Koss, M. J., et al. 2017, *ApJS*, 233, 17, doi: [10.3847/1538-4365/aa96ad](https://doi.org/10.3847/1538-4365/aa96ad)
- Richards, E. E., van Zee, L., Barnes, K. L., et al. 2016, *MNRAS*, 460, 689, doi: [10.1093/mnras/stw1016](https://doi.org/10.1093/mnras/stw1016)
- Riffel, R. A., Storchi-Bergmann, T., Winge, C., et al. 2008, *MNRAS*, 385, 1129, doi: [10.1111/j.1365-2966.2008.12936.x](https://doi.org/10.1111/j.1365-2966.2008.12936.x)
- Riley, A. 2017, *STIS Instrument Handbook for Cycle 25, Version 16.0* (Space Telescope Science Institute)
- Robinson, J. H., Bentz, M. C., Courtois, H. M., et al. 2021, arXiv e-prints, arXiv:2103.07000, <https://arxiv.org/abs/2103.07000>
- Rodríguez-Ardila, A., & Viegas, S. M. 2003, *MNRAS*, 340, L33, doi: [10.1046/j.1365-8711.2003.06538.x](https://doi.org/10.1046/j.1365-8711.2003.06538.x)
- Rosario, D. J., Shields, G. A., Taylor, G. B., Salviander, S., & Smith, K. L. 2010, *ApJ*, 716, 131, doi: [10.1088/0004-637X/716/1/131](https://doi.org/10.1088/0004-637X/716/1/131)
- Rupke, D. S., Veilleux, S., & Sanders, D. B. 2005, *ApJS*, 160, 87, doi: [10.1086/432886](https://doi.org/10.1086/432886)
- Rupke, D. S. N., Gültekin, K., & Veilleux, S. 2017, *ApJ*, 850, 40, doi: [10.3847/1538-4357/aa94d1](https://doi.org/10.3847/1538-4357/aa94d1)
- Sani, E., Lutz, D., Risaliti, G., et al. 2010, *MNRAS*, 403, 1246, doi: [10.1111/j.1365-2966.2009.16217.x](https://doi.org/10.1111/j.1365-2966.2009.16217.x)
- Sani, E., Davies, R. I., Sternberg, A., et al. 2012, *MNRAS*, 424, 1963, doi: [10.1111/j.1365-2966.2012.21333.x](https://doi.org/10.1111/j.1365-2966.2012.21333.x)
- Schmitt, H. R., Donley, J. L., Antonucci, R. R. J., et al. 2003, *ApJ*, 597, 768, doi: [10.1086/381224](https://doi.org/10.1086/381224)
- Schmitt, H. R., & Kinney, A. L. 1996, *ApJ*, 463, 498, doi: [10.1086/177264](https://doi.org/10.1086/177264)
- Sellwood, J. A., & Spekkens, K. 2015, arXiv e-prints, arXiv:1509.07120, <https://arxiv.org/abs/1509.07120>
- Sersic, J. L. 1968, *Atlas de Galaxias Australes*
- Shen, Y., Liu, X., Greene, J. E., & Strauss, M. A. 2011, *ApJ*, 735, 48, doi: [10.1088/0004-637X/735/1/48](https://doi.org/10.1088/0004-637X/735/1/48)
- Shuder, J. M., & Osterbrock, D. E. 1981, *ApJ*, 250, 55, doi: [10.1086/159347](https://doi.org/10.1086/159347)
- Smithsonian Astrophysical Observatory. 2000, SAOImage DS9: A utility for displaying astronomical images in the X11 window environment. <http://ascl.net/0003.002>
- Spekkens, K., & Sellwood, J. A. 2007, *ApJ*, 664, 204, doi: [10.1086/518471](https://doi.org/10.1086/518471)
- Storchi-Bergmann, T., Lopes, R. D. S., McGregor, P. J., et al. 2010, *MNRAS*, 402, 819, doi: [10.1111/j.1365-2966.2009.15962.x](https://doi.org/10.1111/j.1365-2966.2009.15962.x)
- Storchi-Bergmann, T., Dall'Agnol de Oliveira, B., Longo Micchi, L. F., et al. 2018, *ApJ*, 868, 14, doi: [10.3847/1538-4357/aae7cd](https://doi.org/10.3847/1538-4357/aae7cd)
- Suganuma, M., Yoshii, Y., Kobayashi, Y., et al. 2006, *ApJ*, 639, 46, doi: [10.1086/499326](https://doi.org/10.1086/499326)
- Terzić, B., & Graham, A. W. 2005, *MNRAS*, 362, 197, doi: [10.1111/j.1365-2966.2005.09269.x](https://doi.org/10.1111/j.1365-2966.2005.09269.x)
- Tody, D. 1986, in *Society of Photo-Optical Instrumentation Engineers (SPIE) Conference Series*, Vol. 627, Proc. SPIE, ed. D. L. Crawford, 733, doi: [10.1117/12.968154](https://doi.org/10.1117/12.968154)

- Tody, D. 1993, in *Astronomical Society of the Pacific Conference Series*, Vol. 52, *Astronomical Data Analysis Software and Systems II*, ed. R. J. Hanisch, R. J. V. Brissenden, & J. Barnes, 173
- Trindade Falcão, A., Kraemer, S. B., Fischer, T. C., et al. 2020, *MNRAS*, doi: [10.1093/mnras/staa3239](https://doi.org/10.1093/mnras/staa3239)
- Unger, S. W., Pedlar, A., Axon, D. J., et al. 1987, *MNRAS*, 228, 671, doi: [10.1093/mnras/228.3.671](https://doi.org/10.1093/mnras/228.3.671)
- van Dokkum, P. G. 2001, *PASP*, 113, 1420, doi: [10.1086/323894](https://doi.org/10.1086/323894)
- van Dyk, S. D., Hamuy, M., & Filippenko, A. V. 1996, *AJ*, 111, 2017, doi: [10.1086/117937](https://doi.org/10.1086/117937)
- Van Rossum, G., & Drake, F. L. 2009, *Python 3 Reference Manual* (Scotts Valley, CA: CreateSpace)
- Veilleux, S. 1991, *ApJ*, 369, 331, doi: [10.1086/169765](https://doi.org/10.1086/169765)
- Veilleux, S., Bolatto, A., Tombesi, F., et al. 2017, *ApJ*, 843, 18, doi: [10.3847/1538-4357/aa767d](https://doi.org/10.3847/1538-4357/aa767d)
- Veilleux, S., & Osterbrock, D. E. 1987, *ApJS*, 63, 295, doi: [10.1086/191166](https://doi.org/10.1086/191166)
- Verheijen, M. A. W., & Sancisi, R. 2001, *A&A*, 370, 765, doi: [10.1051/0004-6361:20010090](https://doi.org/10.1051/0004-6361:20010090)
- Weisenburger, K. L., Huehnerhoff, J., Levesque, E. M., & Massey, P. 2017, *Journal of Open Source Software*, 2, 102, doi: [10.21105/joss.00102](https://doi.org/10.21105/joss.00102)
- Wolfram Research, I. 2014, *Mathematica*, Version 10.0. <https://www.wolfram.com/mathematica>
- Wylezalek, D., Flores, A. M., Zakamska, N. L., Greene, J. E., & Riffel, R. A. 2020, *MNRAS*, 492, 4680, doi: [10.1093/mnras/staa062](https://doi.org/10.1093/mnras/staa062)
- Yang, Z., Bian, W.-H., & Wang, Y. 2013, *Ap&SS*, 348, 517, doi: [10.1007/s10509-013-1566-3](https://doi.org/10.1007/s10509-013-1566-3)
- Yuan, W., Macri, L. M., Peterson, B. M., et al. 2020, *arXiv e-prints*, arXiv:2012.05931. <https://arxiv.org/abs/2012.05931>
- Zhu, L., Zhang, S. N., & Tang, S. 2009, *ApJ*, 700, 1173, doi: [10.1088/0004-637X/700/2/1173](https://doi.org/10.1088/0004-637X/700/2/1173)